A Predictive Framework for Thermomechanical Fatigue Life of High Silicon Molybdenum Ductile Cast Iron Based on Considerations of Strain Energy Dissipation

by

Katherine R. Avery

A dissertation submitted in partial fulfillment
of the requirements for the degree of
Doctor of Philosophy
(Mechanical Engineering)
in The University of Michigan
2016

Doctoral Committee:

Professor Jwo Pan, Co-Chair
Carlos Carvalho Engler-Pinto Jr., Co-Chair
Professor J. Wayne Jones
Professor Wei Lu

© Katherine R. Avery 2016
All Rights Reserved

To Ray and Molly

"What lies behind us, and what lies before us,
are small matters
compared to what lies within us."
- Emerson

ACKNOWLEDGEMENTS

This thesis represents the culmination of one journey, and the start of a wonderful new one. At this juncture, I would be remiss if I did not recognize the individuals who were so instrumental to my growth and discovery. Many thanks go to my adviser, Dr. Jwo Pan, for his guidance and support throughout my graduate education. He has enabled my growth in new and exciting directions, and has helped me to form connections that have allowed me to grow as a researcher. I have no doubt that his influence will remain long through my career. I would like to express my appreciation to my committee members at the University of Michigan, Professor Wayne Jones and Professor Wei Lu, for generously offering their time, support, guidance and good will throughout the preparation and review of this document.

My sincerest gratitude goes to Dr. Carlos Engler-Pinto at Ford for serving as co-chair of my dissertation committee, and for being my primary research adviser for the past four years. This project is deeply rooted in his influence and I am very grateful for the opportunity to work with him on the challenging research questions addressed in this dissertation. Beyond the incredible breadth of intellectual support he has given my project, he has shown exemplary mentorship and encouragement; without these, I surely would have failed to achieve this goal. My thanks are not enough to show the depth of my appreciation.

Also at Ford, my thanks go to Dr. Xuming Su for the steadfast support he has given this project over the years. His continued interest in my professional growth has been instrumental as I establish my career and I look forward to many more successful

collaborations. I wish to thank my many colleagues at Ford who have provided their assistance and insight to the project over the years, including Dr. James Boileau, Mr. Jim Gavulic, Mr. Hailong Zhao, and Dr. Martin Jones.

Completing my dissertation has required far more than academic support, and I have many, many people to thank for their guidance and patience over the course of this journey. In particular, I would like to thank my lab mates at the University of Michigan, Dr. Teresa Rinker and Dr. William Lai, for their insight and advice. To all my friends and colleagues who have served as my advocates, counselors and co-conspirators, thank for you for your unwavering belief in my success. You have helped me to push through each challenge and come out stronger on the other side. I would like to thank my family for showing me how to live with courage, and how to use every unexpected setback as an opportunity to grow. You may not realize it every day, but you each are a constant inspiration to me.

Finally, thanks go to my partner and foremost supporter, Dr. Steven Vozar. I cannot even begin to express my gratitude and appreciation for your friendship. Thank you for tolerating the late nights and roller coaster of emotion these last few months have brought as I close out this chapter of life. Your patience and support are as stabilizing as they are rejuvenating, and I look forward to anything and everything that comes next.

TABLE OF CONTENTS

LIST OF FIGURES

Figure

LIST OF TABLES

Table

ABSTRACT

A Predictive Framework for Thermomechanical Fatigue Life of High Silicon Molybdenum Ductile Cast Iron Based on Cyclic Inelastic Energy Dissipation

by

Katherine R. Avery

Co-Chairs: Professor Jwo Pan and Doctor Carlos Engler-Pinto Jr.

Isothermal low cycle fatigue (LCF) and anisothermal thermomechanical fatigue (TMF) tests were conducted on a high silicon molybdenum (HiSiMo) cast iron for temperatures up to 1073K. LCF and out-of-phase (OP) TMF lives were significantly reduced when the temperature was near 673K due to an embrittlement phenomenon which decreases the ductility of HiSiMo at this temperature. In this case, intergranular fracture was predominant, and magnesium was observed at the fracture surface. When the thermal cycle did not include 673K, the failure mode was predominantly transgranular, and magnesium was not present on the fracture surface. The in-phase (IP) TMF lives were unaffected when the thermal cycle included 673K, and the predominant failure mode was found to be transgranular fracture, regardless of the temperature. No magnesium was present on the IP TMF fracture surfaces. Thus, the embrittlement phenomenon was found to contribute to fatigue damage only when the temperature was near 673K and a tensile stress was present.

To account for the temperature- and stress-dependence of the embrittlement phenomenon on the TMF life of HiSiMo cast iron, an original model based on the cyclic

inelastic energy dissipation is proposed which accounts for temperature-dependent differences in the rate of fatigue damage accumulation in tension and compression. The proposed model has few empirical parameters. Despite the simplicity of the model, the predicted fatigue life shows good agreement with more than 130 uniaxial low cycle and thermomechanical fatigue tests, cyclic creep tests, and tests conducted at slow strain rates and with hold times. The proposed model was implemented in a multiaxial formulation and applied to the fatigue life prediction of an exhaust manifold subjected to severe thermal cycles. The simulation results show good agreement with the failure locations and number of cycles to failure observed in a component-level experiment.

CHAPTER I

Introduction

Following a global energy crisis in 1973, the United States congress enacted the Energy Policy and Conservation Act (EPCA) of 1975 in an effort to reduce energy demand and improve the supply and production of domestic sources of energy (*National Highway Traffic Safety Administration*, 2014). Most notably, the EPCA established the Strategic Petroleum Reserve, the Energy Conservation Program for Consumer Products, and Corporate Average Fuel Economy (CAFE) regulations. CAFE requires that automakers produce vehicles that meet or exceed a target on fuel economy (miles per gallon) when averaged across their entire fleet, weighted by production (*National Highway Traffic Safety Administration*, 2014). Manufacturers that fail to meet CAFE targets must pay a monetary penalty on a per-vehicle basis (*Office of Transportation and Air Quality*, 2012). CAFE standards are regulated by the National Highway Traffic Safety Administration and, since 2007, the Environmental Protection Agency (EPA) on behalf of the U.S. Department of Transportation.

Aggressive CAFE targets were recently set for each model year out to 2025, when automakers must achieve 54.5 miles per gallon across their fleets (*Office of the Press Secretary*, 2012). The 2025 target represents a significant increase in fuel economy from the current sales-weighted fuel economy of 25.4 miles per gallon as of January 2015 (*Sivak and Schoettle*, 2015). Automakers have responded to the increasingly

stringent demands by implementing comprehensive packages of total vehicle technologies that improve vehicle efficiency and reduce energy use. The most prominent among these are vehicle lightweighting, to increase the use of lightweight metals and polymers in vehicles; waste heat recovery systems, to convert engine heat to electricity to power auxiliary systems; and powertrain technologies, to improve the efficiency of power generation and transmission.

Powertrain technologies in the engine make the generation of power more efficient. Direct injection and turbocharging are two key engine technologies that are increasingly deployed, among other proprietary advances. The resulting fuel economy improvements can be considerable. For example, in 2008, Ford introduced the EcoBoost engine, which leverages many technologies, including direct injection and turbocharging, to achieve a 20 % improvement in fuel efficiency and a 15 % reduction in greenhouse gas emissions when compared to larger, naturally-aspirated engines of the same power and torque output (*National Highway Traffic Safety Administration*, 2008).

These newer engine technologies, in promoting more complete combustion of fuel, can result in higher temperatures of the exhaust gas. While this is beneficial to improve converter light-off and reduce emissions output, it can also increases the temperature of the downstream exhaust and emissions components, and poses a unique challenge to the durability of the structural materials in these applications. The turbocharger housing and exhaust manifold are in closest proximity to the cylinder, and inlet temperatures to these systems can reach 950 °C or higher depending on the compression ratio, engine configuration and other technologies employed (*Simon et al.*, 2000). Due to the non-uniform heating and cooling imposed on these components, temperature gradients exist; their severity depends on, among other factors, the thermal conductivity of the material, the duration of exposure to the hot exhaust gas and the use of additional cooling or heat shielding mechanisms.

1.1 Thermomechanical Fatigue of Exhaust Manifold

During normal operation of a vehicle, the engine cycles irregularly between off, idle and full-power conditions, in transient "start-stop" cycles. Since the exhaust gas temperature varies with the power output of the engine, the application of start-stop cycles causes cyclic variation in the temperature experienced by the exhaust manifold. The transient application of thermal gradients causes thermally-generated mechanical strains which vary cyclically, and are coupled with additional high temperature damage mechanisms, like oxidation and creep. This type of fatigue is widely known as "thermal-mechanical" or "thermomechanical" fatigue. *Jaske* (1976) showed that the conditions of thermomechanical fatigue (TMF) can significantly reduce durability when compared to isothermal application of the same cyclic strain or stress.

The coupled thermal and mechanical loads which are characteristic of TMF have shown to have a prominent effect on the durability of the exhaust manifold. Figure 1.1a shows a manifold which has undergone component-level validation testing under conditions of severe thermal cycling in an accelerated dynamometer test for component validation. The transient thermal gradients generated a mechanical strain due to the constraint of hot material by the surrounding cooler material, and the manifold experienced a through-crack at the location denoted in Figure 1.1a within a short number of cycles. The fracture surface of the crack is shown in Figure 1.1b. The crack propagated quickly and allowed exhaust gas to escape, which led to the detection of the crack. Upon further examination, additional cracks were detected at additional locations on the outer surface of the manifold. It is therefore imperative to understand the durability of high temperature engine components undergoing TMF to achieve a reliable design.

(a)

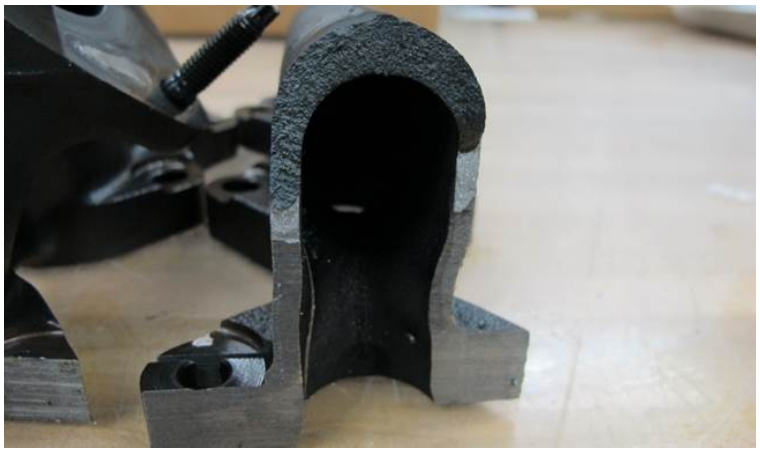

(b)

Figure 1.1: Cast iron manifold subjected to severe thermal cycles during a dynamometer tests that resulted in (a) a large crack that propagated (b) through the thickness of the manifold wall.

1.2 Predictive Tools for TMF Durability

The use of predictive technologies that can accurately represent the detrimental effect of transient thermal gradients can significantly reduce the time and expense needed to achieve a durable design. As demonstrated in a 1991 literature review by *Halford*, a plethora of models exist in in the literature for predicting the high temperature fatigue, fatigue-oxidation and creep-fatigue performance of engineering materials. Nearly all proposed models have shown applicability to a specific data set; however, most lack the generality that could allow them to be accurately employed outside the range of conditions or materials for which they were developed. Furthermore, the generalization of a high-temperature damage criteria to conditions of thermal cycling is not a trivial process, and it presently cannot be known *a priori* which damage mechanisms are most active during an anisothermal cycle, or at what temperature a failure criterion could be applied (*Karasek et al.*, 1988).

Neu and Sehitoglu (1989b) proposed a comprehensive model which linearly sums the damage due to fatigue, oxidation and creep. In the dissertation work, this model has been applied to the exhaust manifold application with a candidate cast iron material. However, it fails to provide a good estimate for the key damage mechanism observed in the cast iron which shows to be highly relevant to the TMF life, which is the sulfur embrittlement of grain boundaries at 400 °C. Furthermore, it is a cumbersome model with many empirical parameters and material constants that must be determined. As such, it is does not provide an attractive solution for industry-focused predictive efforts of thermomechanical fatigue life.

1.3 Contributions of the Dissertation

The main contributions of this dissertation will help to overcome the challenges faced in predicting the thermomechanical fatigue life of a candidate material for a cast

automotive exhaust manifold application. The first contribution is the most comprehensive, single-source database of high temperature durability data on a candidate material for the automotive exhaust manifold application, including isothermal fatigue, creep, cyclic creep and anisothermal TMF. This experimental work is reported in Chapter II and Chapter III.

The second contribution is a thorough and detailed investigation of the physical mechanisms which cause damage in high temperature fatigue and thermomechanical fatigue of the material, with special consideration of the effect of an embrittlement phenomenon that was observed at intermediate temperatures. For the isothermal case, this work is reported in Chapter II, while Chapter III details the observations made in the case of thermomechanical fatigue for varying thermal range, phasing and hold times.

The third contribution of this dissertation is a robust method to predict the TMF life of the candidate material under conditions of severe thermal cycling. The predictive framework, which is based on consideration of inelastic strain energy dissipation, is developed in Chapter IV. The proposed method relies on the stabilized stress-strain response, and the physically-informed relationship between damages occurring from the relevant failure mechanisms. As such, it involves few empirical constants to achieve a good estimate of thermomechanical fatigue life, thus improving its suitability for use in an industry-focused setting.

1.4 Structure of the Dissertation

The remainder of the dissertation is structured in the following manner: Chapter II describes the structural cast iron material discussed in the dissertation, and explains the isothermal tensile and low cycle fatigue experiments conducted to characterize the high-temperature performance of the material. Optical and scanning electron microscopy are conducted on tested specimens to understand the dependence of the

mechanism activation on both temperature and strain range. Particular attention is paid to an embrittlement phenomenon that is observed at intermediate temperatures.

Extensive thermomechanical fatigue tests are described in Chapter III. The strain-life results and stress-strain behavior are presented, along with a detailed investigation of the fractography conducted to characterize the active predominant damage mechanisms as related to the temperature range of the thermal cycle. The isothermal and anisothermal damage mechanisms are compared. The intermediate temperature embrittlement is found to play a critical role in reducing durability in conditions of both isothermal and anisothermal cycling.

Chapter IV provides a review of commonly-used high-temperature fatigue criteria, and applies a state-of-the-art mechanism-based model to predict the thermomechanical fatigue life of the cast iron material. In general, the fatigue life prediction provided by the TMF model is adequate. However, when the embrittlement phenomenon is found to be damaging, the fatigue life prediction is severely overpredicted.

In Chapter V, a new predictive method, based on the inelastic strain energy dissipation, is proposed that accounts for a temperature-dependent difference in the rate at which damage accumulates under tensile and compressive stress states. The model achieves good correlation with the uniaxial fatigue, cyclic creep and thermomechanical fatigue data generated for the dissertation work. The new predictive framework is implemented in a multiaxial formulation and applied to a component-level life prediction. The proposed method shows good agreement with the fatigue life and critical locations where cracks were found during a physical test.

Finally, Chapter VI summarizes the conclusions reached in the dissertation work and proposes future work.

CHAPTER II

Material Characterization

Portions of this chapter have been published in *Avery et al.* (2015).

2.1 Requirements for Materials in the Exhaust Manifold Application

The primary function of an exhaust manifold is to consolidate the exhaust gas streams from each cylinder into a single stream that passes through the vehicle's exhaust management and emissions controls systems. The manifold operates in a severe environment due to the high heat experienced from its close proximity to the cylinders. Additionally, severe, transient thermal gradients exist due to the non-uniform heating and cooling of the component. Consideration of these challenges must be made when selecting a material for the exhaust manifold application, along with typical requirements of manufacturability and cost. Summarily, the suitability of the material for an exhaust manifold application depends on the following characteristics of the material:

1. Resistance to vibrational (high cycle) fatigue
2. Damping characteristics for Noise, Vibration and Harshness (NVH)
3. Resistance to corrosion
4. Available manufacturing processes

5. Suitable cost
6. Coefficient of thermal expansion and thermal conductivity
7. Resistance to thermal shock
8. Resistance to creep and oxidation
9. Resistance to thermomechanical fatigue and thermal fatigue
10. Stability of microstructure up to maximum operating temperature

2.1.1 High Cycle Fatigue, NVH and Corrosion Requirements

The most common set of performance requirements on materials in the automotive sector are to have good resistance to vibrational (high cycle) fatigue, good damping characteristics to reduce NVH, and good resistance to corrosion from salts. In particular, the resistance to vibrational fatigue and corrosion are prominent considerations in the development of alloys for a wide range of automotive applications. These requirements additionally apply to the exhaust manifolds.

2.1.2 Manufacturing and Cost

Manifolds can be manufactured by casting or fabrication. Fabricated manifolds readily preserve heat in the exhaust gas stream, allowing for quicker converter light-off, and are significantly lighter than cast manifolds. Fabricated manifolds are helpful to optimize engine performance by individually venting each cylinder; however, they require the introduction of additional manufacturing processes, such as stamping, pipe-bending and welding, which are generally not required for cast manifolds.

Cast manifolds are less expensive to produce and have a small envelope size in the engine compartment. They can also be designed to easily support other downstream components, such as turbochargers. The trade-off is that they can have significant weight, and can suffer a greater degree of thermal fatigue and thermomechanical fatigue due to the thick wall sections they require.

Cast manifolds currently provide the lowest-cost solution for the high production volumes required in the manufacturing of passenger vehicles. Alloys have been specifi-

cally developed to reduce the cost of materials for casting, while improving castability, and fatigue and corrosion resistance.

2.1.3 Thermal Properties

Favorable thermal conductivity improves the soaking time required to achieve a stabilized thermal gradients in the manifold. This, in turn, increases the ability of the manifold to preserve heat in the exhaust gas stream more quickly. Additionally, the material should have a fairly low coefficient of thermal expansion to improve the long-term quality of the seal between the manifold and engine block, and to reduce the likelihood for thermal and thermomechanical fatigue.

2.1.4 High Temperature Damage Resistance

High temperature damage mechanisms include microstructural instability, creep, oxidation, and thermomechanical fatigue. The susceptability of a design to these modes of damage depends in part on the conditions of use and the geometry of the component. Ultimately, the resistance to changes in the microstructure, and damage by creep, oxidation, fatigue and thermomechanical fatigue is determined by the material characteristics.

2.2 Description of Cast Iron Material

2.2.1 Generalities

Ductile cast iron (DCI), or nodular cast iron, was patented in 1949 and has become an important engineering material for casting in nearly every industry sector (*Millis*, 1949). Nodular cast iron is named for its spherical graphite particles, which offer greater ductility, toughness and strength than the graphite flakes which form in gray cast iron. The nodular form of graphite is achieved by the addition of certain alloying

elements, including magnesium and silicon, in a process known as "inoculation". Most of the inoculant is added during the melt stage, and small additions are often made in the pour or cast stages to fine-tune the chemistry. The size and distribution of nodules is primarily controlled by cooling of the casting. Nodules are characterized by size (diameter), nodularity (a measure of average roundness) and count per unit area (distribution) (*ASTM E2567*, 2014).

DCI is a cast material which is well-suited for a wide variety of corrosive or oxidizing applications. The matrix can be produced in any typical iron crystallographic structure, with the most common being ferritic or pearlitic, or a mix of the two; ductile irons can also feature an "ausferrite" matrix which is a mix of acicular ferrite and carbon-stabilized austenite (*Ductile Iron Society*, 1998). A ferritic matrix can be achieved with fewer alloying elements, resulting in lower cost, and provides good strength, high ductility, and a relatively low coefficient of thermal expansion. Consequently, a ferritic matrix structure is widely used in high-volume automotive exhaust applications.

The composition of DCI has been standardized into three grades in *SAE J2582* (2001) according to the content of silicon and molybdenum. The specified content of silicon is between 3.50 and 4.50 %, while the molybdenum content has allowable ranges for each grade as

Grade 1: 0.50 wt% maximum
Grade 2: 0.51–0.70 wt%
Grade 3: 0.71–1.00 wt%

DCI containing 4 to 6 % (weight) of silicon (Si) and up to 2 % molybdenum (Mo) is known as HiSiMo DCI. HiSiMo DCI is characterized by good high-temperature strength, and moderate resistance to creep and oxidation (*Davis*, 1996; *Goodrich*, 2003; *Elliott*, 1988).

The high silicon content increases oxidation resistance of DCI through the formation of a silicon-rich surface layer. Furthermore, the maximum operating temperature

of HiSiMo DCI is limited by the transformation temperature of ferrite to austenite, which typically occurs near 723 °C in an iron-carbon system. Sufficient additions of silicon can stabilize a ferrite matrix by suppressing the transformation temperature to the range of 810 to 840 °C; HiSiMo DCI is typically used up to a maximum temperature of about 810 °C (*Sponseller et al.*, 1968; *Li et al.*, 2004). DCI containing more than 6 % silicon is generally too brittle for use in practical engineering applications (*Ductile Iron Society*, 1998).

Molybdenum is known to significantly elevate the high temperature tensile strength and creep and creep-rupture strength of DCI (*Davis*, 1996). Molybdenum content up to 2 % in high silicon ductile iron is very effective in increasing resistance to thermal fatigue and creep, as well as tensile strength, due to the formation of a cell-like network of molybdenum carbides at grain the boundaries (*Park et al.*, 1987; *Ductile Iron Society*, 1998; *Li et al.*, 2004; *Park et al.*, 2005). Further additions of molybdenum beyond 2 % increases the segregation of grain boundary carbides beyond a useful level, resulting in reduced ductility and insufficient carbon available for graphite formation (*Adewara and Loper*, 1975; *Ductile Iron Society*, 1998). Particularly when pearlite-stabilizing elements are present (including aluminum, manganese and copper), molybdenum content should not exceed 2 %. Carbide content is typically controlled to 5 % or less to minimize the detrimental effects of carbides on properties and machinability, and to maximize the carbon available for to form graphite (*Davis*, 1996).

In light of these attributes, ferritic HiSiMo DCI is well-suited to the requirements imposed by the automotive exhaust manifold application, and is the one of the most commonly used for exhaust manifolds and turbocharger housings (*Weber et al.*, 1998).

2.2.2 Material Processing and Microstructure

The high-silicon molybdenum ductile cast iron investigated in the present study is purchased as stock material from Wescast Industries Incorporated, in Brantford, Ontario. The following process was used to produce the material for the present study (*Quan*, 2015):

Keel blocks were cast in chemically-bonded sand molds at the Richard W. Levan Technical Centre of Wescast. Heats weighing approximately 100 kg were made using a 350 kW coreless induction furnace operating at 1 kHz. Conventional treatment was used. Following compositional adjustments, the alloy was poured in the temperature range of 1390 to 1460 °C to a ladle. A coarse-grained granular ferrosilicon-magnesium nodulizer was added, along with a fine-grained ferrosilicon inoculant. Bars with dimensions of approximately 15 × 15 × 150 mm were cast in chemically-bonded sand molds. Further additions of the fine-grained ferrosilicon inoculation were made, and the bars were allowed to naturally cool to near-ambient temperature prior to removal from the mold, which facilitates the formation of as-cast ferrite. No heat treatment was used.

The chemical composition of the DCI alloy considered in the dissertation work was measured by Element Wixom in Wixom, MI. The reported composition values are shown in Table 2.1. Based on the silicon and molybdenum contents, the material is Grade 1 (*SAE J2582*, 2001). The carbon and sulfur contents were measured in accordance with *ASTM E1019* (2011). The content of the other elements was measured by glow discharge optical emission spectrometry (GD-OES) according to an Element Wixom Standard Operating Procedure, *SOP CH-IO-002*, which was based on a number of standards for measuring atomic content by GD-OES in various materials, including *ASTM E415* (2014), *ASTM E1086* (2011), *ASTM E1251* (2011), and *ASTM E1999* (2011).

The typical as-cast microstructure is shown as-polished under optical microscope

Table 2.1: Chemical composition of the HiSiMo DCI in weight percent.

Element	Weight Percent
C	3.26
S	0.010
Si	4.28
Mo	0.48
P	0.018
Mg	0.032
Mn	0.21
Cr	0.21
Al	0.010
Cu	0.11
Ni	0.05
Ti	0.014
V	<0.005
Sb	<0.005
Sn	0.005
Ce	0.019

in Figure 2.1a. The light phase is the ferrite matrix, and the dark circles in the image are graphite nodules. The nodules have a typical diameter of 20 µm and a maximum observed diameter of 40 µm. The nodularity is 92 %, and the nodule count is approximately 350 mm^{-2}. The nodule content and nodularity were measured by image analysis in accordance with *ASTM E1245* (2008) and *ASTM A247* (2010).

The same material was exposed to a 2 % Nital etch for 30 s in Figure 2.1b to reveal the grain boundaries. The matrix has an average grain diameter of 35 µm as measured by the lineal intercept and comparison methods described in *ASTM E112* (2013). Numerous small shrinkage pores were evident on the cross-section with a typical appearance shown in Figure 2.1c, taken from the location highlighted in Figure 2.1b. Shrinkage pores invariably form in castings during solidification due to the isolation of microvolumes of molten metal in the intergranular space. When the

molten metal finally solidifies, the difference in specific volume between the liquid and solid metal will generate a pore. Shrinkage pores can reduce tensile and fatigue performance by initiating cracks. It is therefore desirable to minimize the size and occurrence of shrinkage pores. The pores visible on a polished cross-section have roughly the same dimension as the ferrite grains.

Dark regions of pearlite and molybdenum carbides (MoC) are clearly visible in the intergranular spaces in Figure 2.1b. The alloy was determined to be 27 % pearlite based on image analysis conducted in accordance with *ASTM E1245* (2008). The The lamellae, clearly visible in Figure 2.1b, are broken due to the self-annealing nature of this HiSiMo DCI, which is cooled slowly to promote the formation of ferrite. The interlamellar spacing is approximately 500 to 600 nm as measured with SEM, making this a fairly fine pearlite structure. It is important to note that this measure of the interlamellar spacing gives a rough approximation. Accurate measures should be obtained by careful transmission electron microscopy (TEM) evaluation. Energy dispersive spectroscopy (EDS) performed on the dark intergranular regions of pearlite revealed a significant presence of copper, chromium and manganese, which are pearlite promoters. These elements have relatively low melting points and tend to collect in the intergranular space during solidification.

Non-destructive examination (NDE) was conducted at Ford Motor Company's Non-Destructive Evaluation lab in Livonia, MI, on randomly-selected cast bars. The purpose was to locate and assess large pores, if any, from the casting process which might affect the results of strength and durability tests. Ten bars were subjected to X-ray radiation with a source voltage of 320 keV and a source current of 2.5 mA. The bars were scanned with the long dimension perpendicular to the X-ray source and detector. An amorphous silicon flat panel detector was used with a Lanex regular scintillator with an area of 127 µm of square pixels. The integration time was 0.4 s. A 6 mm copper filter was used to harden the X-ray beam prior to incidence with

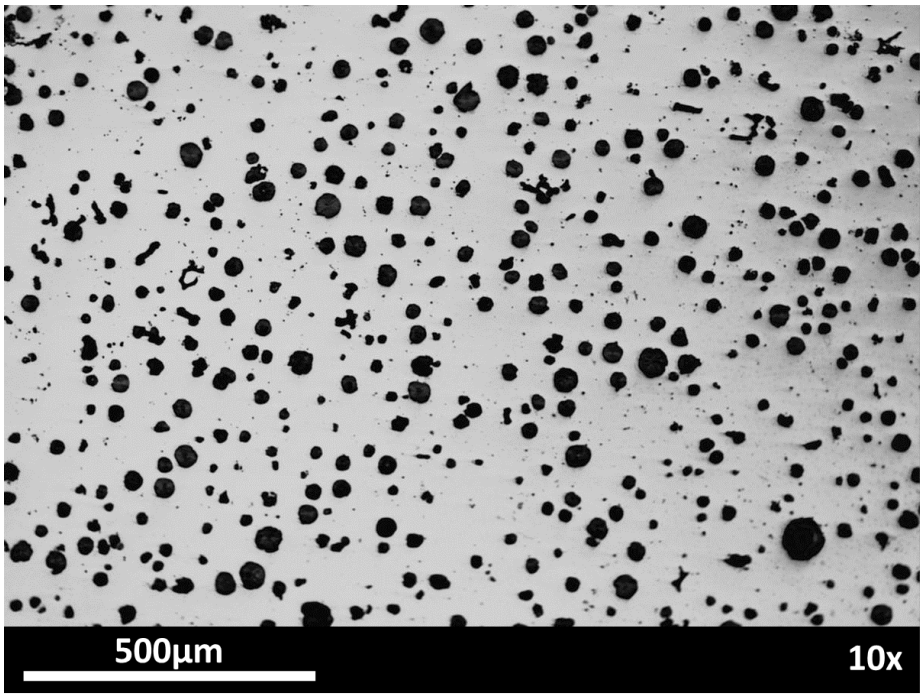

(a)

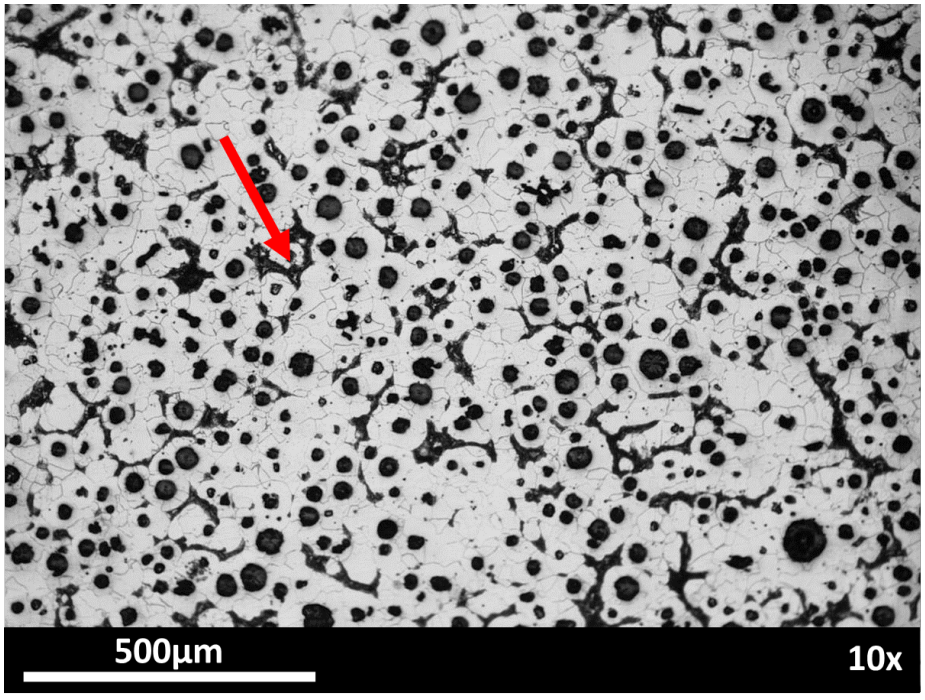

(b)

Figure 2.1: Microstructure of the HiSiMo DCI in the (a) as-polished (optical) and (b) Nital-etched conditions (optical). Continued on next page, (c) a magnified view of a shrinkage pore (SEM) and pearlite in the intergranular region at the location indicated.

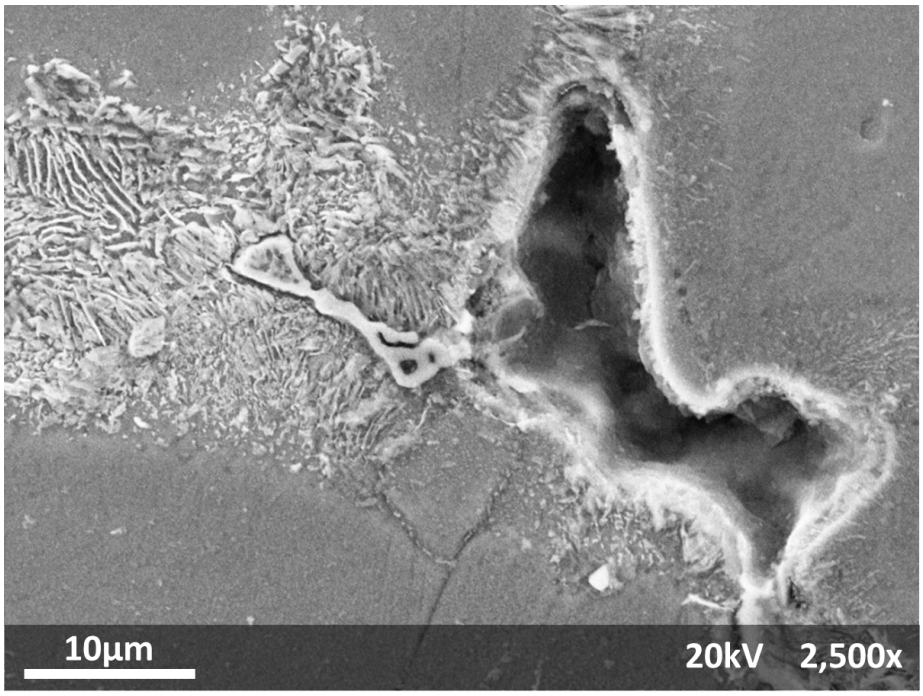

(c)

Figure 2.1: Continued from previous page.

the test bar. The bars were exposed one at a time, and after exposure, the raw radiographs were examined for evidence of internal porosity. The images were also post-processed with a porosity filter to field flatten the image to eliminate changes in thickness with low spatial frequency, and to enhance edges in the image. The resulting filtered images enhanced the appearance of porosity. The minimum defect size which can be detected by this technique is approximately 200 µm.

Raw and porosity-filter radiographs are seen in Figure 2.2 for a representative bar, respectively. Images for all ten bars can be found in Appendix A, Figures A.1 to A.10. The first image shows very slight gradations in color which indicate a thinning of the section due to either internal or external defects. The second image shows the porosity-filtered image where the edges of the specimen show up as thick black lines. No pores were evident in raw radiographs or porosity-filtered radiographs in any of the randomly-selected bars. This suggests that the shrinkage pores seen in the cross-section are comparable are less than 200 µm in dimension.

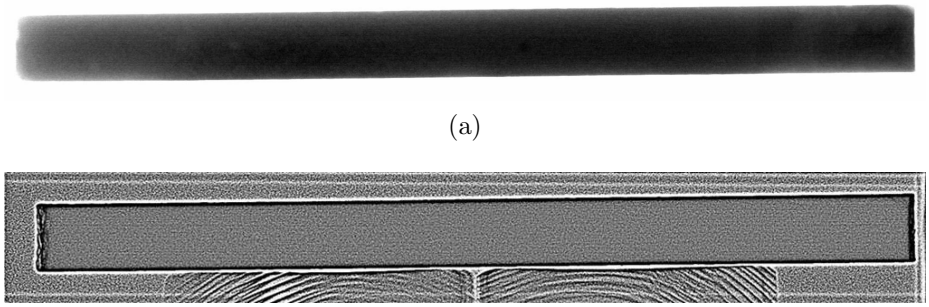

(a)

(b)

Figure 2.2: X-ray images of a cast bar to reveal shrinkage pores greater than 200 µm in size. Raw radiograph image (a) and same image with a porosity filter applied (b). These images are also shown in Figure A.7 in Appendix A.

2.3 Quasi-Static Tensile Characterization

The HiSiMo DCI considered in this study was characterized under quasi-static tensile conditions for temperatures ranging from ambient up to 800 °C. The test procedures and results are described in the following sections, along with fractography to characterize the relevant damage processes under these loading conditions.

2.3.1 Test Procedure

Quasi-static tensile tests were conducted on specimens of HiSiMo DCI to determine the tensile properties of the material, including the elastic (Young's) modulus (E), 0.2 % offset yield (proof) strength, ultimate tensile strength (UTS), elongation and reduction in area. Specimens with a geometry according to *ASTM E2368* (2010) for TMF tests were used to facilitate use of induction heating for tensile tests. Specimens were machined on a lathe from the cast bars, and the ends of the specimens were cut with threads to facilitate placement in the high temperature grips. The specimens for tensile tests were used with an as-machined surface finish. The surface of each specimen was visually inspected and was found to be free from large machining marks or defects. The diameter of each specimen was measured with a shadowgraph at three locations in the reduced section of the specimen, and the average diameter

Figure 2.3: Assembled tensile and TMF specimen and superalloy extensions.

was used for the calculation of stress and reduction of area. The diameter measurements ranged from 7.61 to 7.63 mm with most specimens measuring 7.62 mm. Gauge marks were lightly inscribed 10 mm apart in the gauge length of each specimen, each 5 mm from the longitudinal center of the specimen.

Prior to placement in the test frame, each specimen was assembled with high-temperature nickel-based superalloy extensions to provide enough space between the grips for the induction heating coil. The specimen was locked against the extensions with two stainless steel nuts, one on each end of the specimen, as seen in Figure 2.3.

A servohydraulic MTS frame was used with an Instron 8800 single-axis controller to conduct the tensile tests. A MTS force transducer with a 25 kN capacity, model 661.20A-01, was used. The force transducer was manually aligned in the load train to pass ASTM Class B-2 bending strain targets according to *ASTM E1012* (2014) and *ASTM E83* (2010).

A high-temperature MTS extensometer, model 632.42B-11, with a gauge length of 12.7 mm and a range of $-10/+20$ % was used. Ceramic extension rods were used which had vee-chisel ends to ensure good contact with the specimen surface and

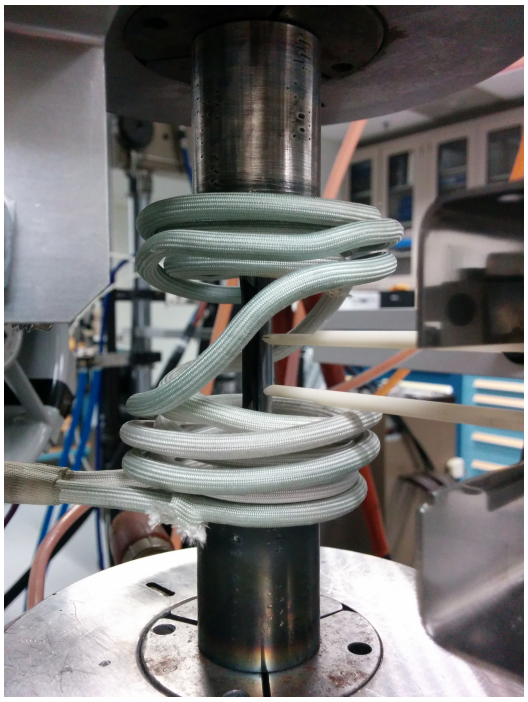

Figure 2.4: Specimen installed in induction coil with high temperature extensometer.

avoid slippage of the extensometer during testing. The extensometer was held in place against the specimen with a spring-loaded arm which applied 300 gram-force through each extension rod. The spring-loaded arm also incorporated a heat shield which further isolated the extensometer from the high temperature of the specimen. The extensometer was carefully placed between the upper and lower portions of the induction coil and seated against the specimen as shown in Figure 2.4. The initial length of the extensometer was recorded at room temperature, and at the test temperature. The extensometer was then balanced to 0 % at the test temperature.

Tensile tests were conducted at room temperature, 300, 400, 500, 600, 700 and 800 °C. Room temperature tests were conducted under ambient conditions at approximately 22 °C. For the elevated temperature tests, heating of the specimen was done by a 5 kW induction heater operating at 250 Hz. The induction coil shown in Figure 2.4 was designed to minimize the temperature gradient along the gauge length to less than ±10 °C. Temperatures were measured through use of two differ-

ent infrared pyrometers focused on the center of the gauge length with a spot size of approximately 6 mm. Specimens were painted with a flat black, high-temperature paint to minimize changes in emissivity during testing which affects the reading from a one-color pyrometer. For tests at 300, 400 and 500 °C, a one-color Raytek pyrometer, model MMMTSSF1L, with a temperature range of -40 to 1100 °C was used. An emissivity setting of 0.875 was used for all tests, as this was shown to correlate well with the temperature measured from a type-K thermocouple welded to the specimen surface at the same location. For tests at 600, 700 and 800 °C, a two-color Raytek pyrometer with a temperature range of 500 to 1100 °C, model number FR1ACF201C, was used. The accuracy of a two-color pyrometer does not depend on the emissivity of the specimen surface.

Tests were conducted under strain control at a rate of $5 \times 10^{-4}\,\mathrm{s}^{-1}$ to a strain of up to 15 %. Tests were stopped at this strain level to protect the extensometer from damage. Once the extensometer was removed, the frame was switched to position-control and the test was continued at a crosshead rate of $5 \times 10^{-3}\,\mathrm{mm\,s}^{-1}$, which provided approximately the same strain rate in the gauge length as the strain-controlled portion of the test. Specimen were pulled at a constant rate until complete separation occurred. Two specimens were tested at each temperature.

Upon completion of the test, the induction heater was turned off and the two halves of the specimen were allowed to cool to room temperature via natural convection and heat transfer to the grips. The specimen halves were then removed from the grips and the superalloy extensions were removed. The two halves of the specimen were carefully placed together and the distance between the gauge marks was measured with a micrometer to the nearest 0.25 mm and the elongation was calculated according to *ASTM E8* (2009). No force was applied to fit the fractured ends together, in compliance with *ASTM E8* (2009) for elongations exceeding 3 %. The elongation measured from this method was verified against the measurement by the extensometer

for tests where the strain did not exceed 15 %. The final diameter was measured at the fractured plane according to *ASTM E8* (2009) and the final area was calculated.

Following testing, the specimen surfaces were examined via optical microscopy to determine the extent of surface and/or oxide cracking. The fracture surfaces were examined with optical and scanning electron microscopy (SEM). SEM analyses were performed with a spot size of 50 and acceleration voltage of 20 kV. Energy dispersive spectroscopy (EDS) was performed on the fracture surfaces to determine the chemical composition present in the crack path. EDS measurements were taken in topographically-similar regions of each fracture surface and are reported as values averaged from at least six measurements. EDS was conducted at a working distance of 10 mm and an acceleration voltage of 20 kV with a detector at an angle of 8° from the longitudinal axis of the sample.

2.3.2 Results

2.3.2.1 Stress-Strain Behavior

The quasi-static engineering stress-strain curves are shown in Figure 2.5. The curves up to 500 °C are plotted on the same ordinate axis, while the tests conducted at 600, 700 and 800 °C are plotted on a with a different scale to accommodate the significantly lower strengths achieved at these temperatures. All of the tensile curves show a linear elastic portion, followed by a clear elastic limit, even at the highest temperatures. A loss of elongation and ductility is clearly observable in the curves at 400 °C. At 500 °C and higher, stress relaxation occurs past the point of yield. Yield (proof) strength was determined by the 0.2 % offset method. Young's Modulus, proof strength and UTS were observed to decrease with increasing temperature, as shown in Figure 2.6.

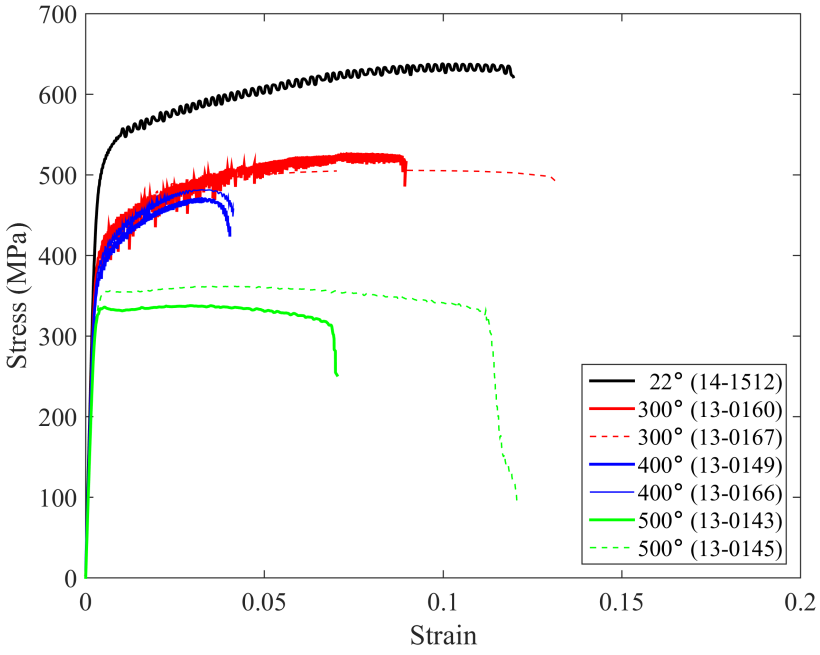

(a)

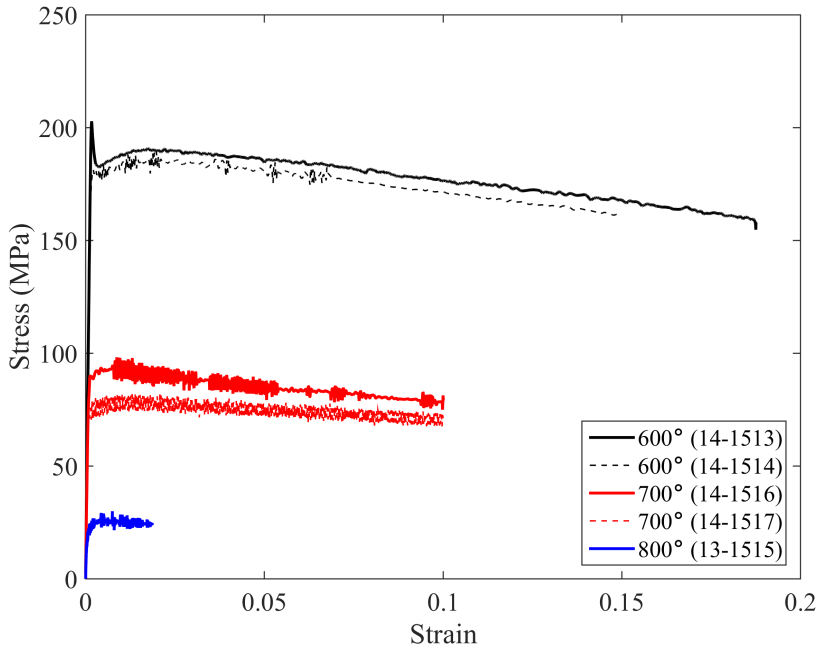

(b)

Figure 2.5: Quasi-static tensile stress-strain curves for tests conducted at a strain rate of $5 \times 10^{-4}\,\mathrm{s}^{-1}$ (a) from room temperature up to 500 °C, and (b) from 600 up to 800 °C. Note the different ordinate scales.

The tensile properties of the HiSiMo DCI investigated in this study are summarized in Table 2.2 for each specimen tested. Elongation at room temperature is found to be about 14 %. When the temperature is increased to 400 °C, the elongation decreased to only 4 %. The change in elongation with temperature is illustrated in Figure 2.7a. The reduction in area correspondingly decreases as the temperature is increased from ambient up to 400 °C, as shown in Figure 2.7b. These two observations signify a loss of ductility occurring in the material at this particular temperature. However, ductility is recovered above 400 °C as demonstrated by an increase in elongation and higher reduction in area. The reduction in area is highest at 800 °C, which is consistent with significant necking occurring at this temperature.

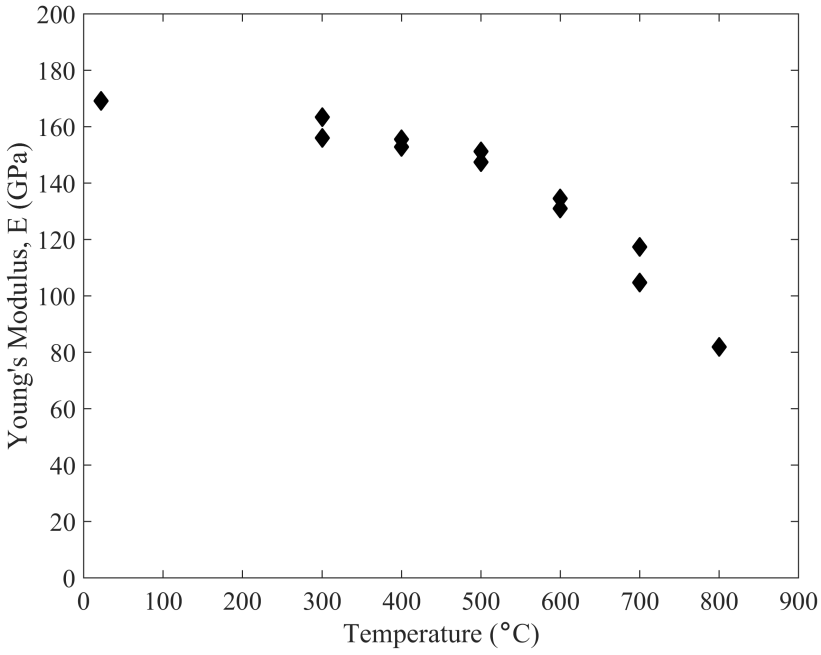

(a)

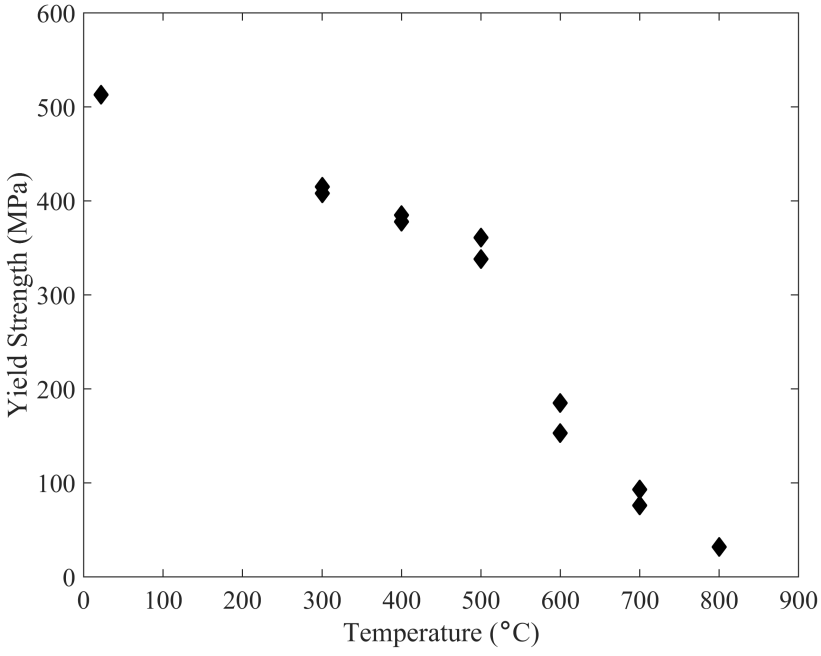

(b)

Figure 2.6: Young's Modulus (a) and yield strength (b) of the HiSiMo DCI determined from quasi-static tests at a strain rate of $5 \times 10^{-4}\,\mathrm{s}^{-1}$ from room temperature up to 800 °C. Continued on next page, (c) tensile strength.

Table 2.2: Tensile properties of the HiSiMo DCI for all tested tensile specimens.

Temp. °C	Specimen No.	E (GPa)	Yield Strength (MPa)	UTS (MPa)	Elongation (%)	Reduction in Area (%)
22	14-1512	169	513	632	14.4	9.0
300	13-0167	163	408	543	13.0	6.7
	13-0160	156	415	527	11.7	6.5
400	13-0164	153	385	481	4.1	2.5
	13-0149	156	378	471	4.6	3.4
500	13-0143	147	338	362	12.4	11.7
	13-0145	151	361	354	10.1	10.0
600	14-1513	131	185	204	28.8	32.0
	14-1514	135	183	180	33.0	32.3
700	14-1516	105	93	98	38.0	39.3
	14-1517	117	76	82	32.6	35.6
800	14-1515	82	32	38	50.1	61.0

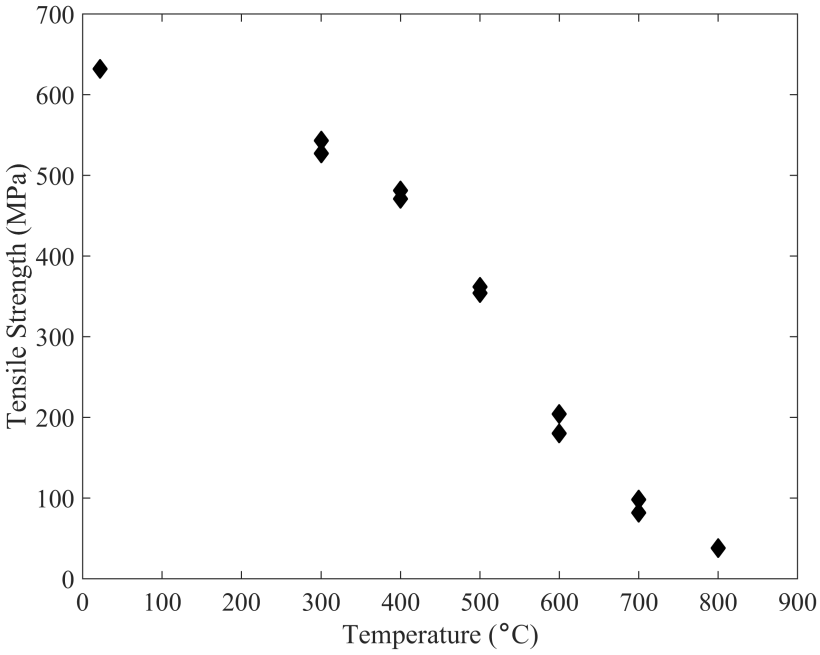

(c)

Figure 2.6: Continued from previous page.

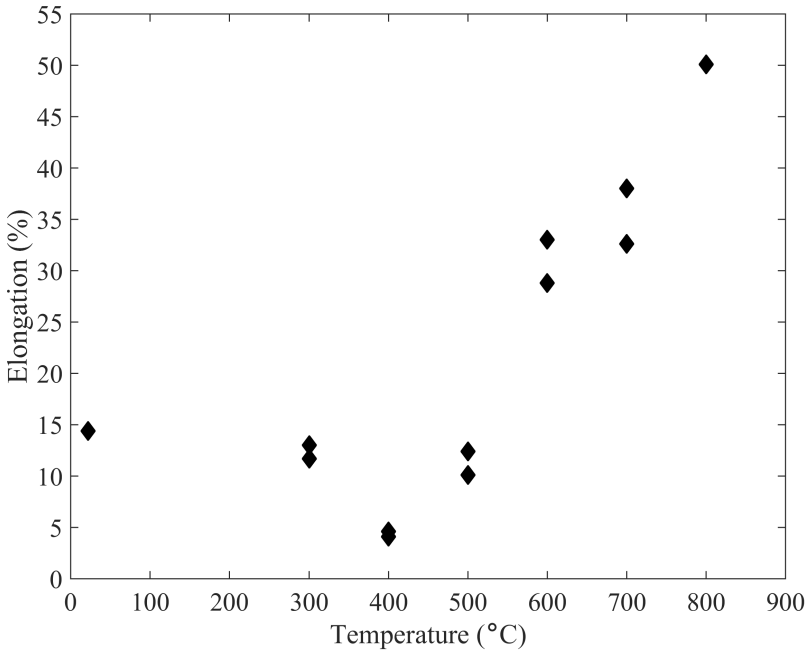

(a)

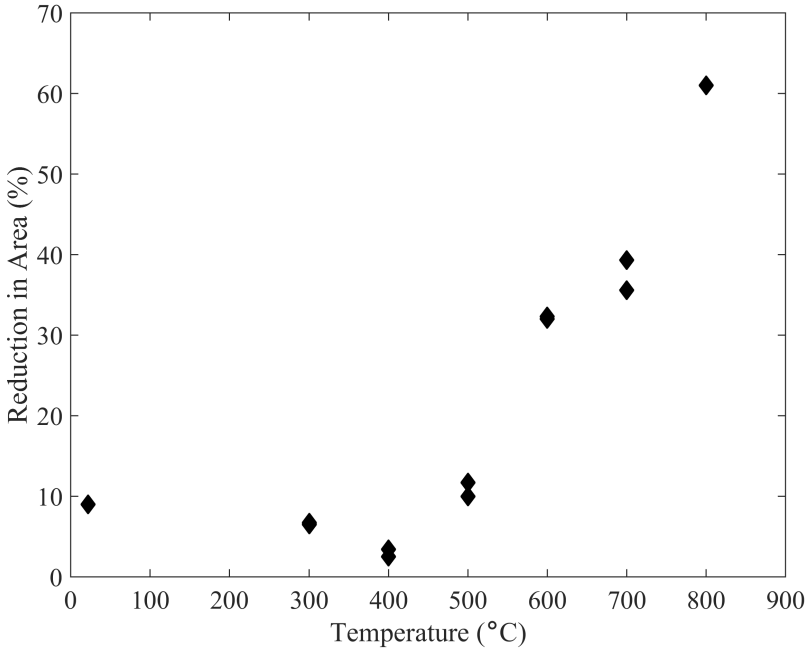

(b)

Figure 2.7: Elongation (a) and reduction of area (b) in tensile specimens tested from room temperature up to 800 °C with a strain rate of $5 \times 10^{-4}\,\mathrm{s}^{-1}$.

2.3.2.2 Observations of Fractured Specimens

A detailed examination of the fracture specimens was conducted to identify the failure modes of HiSiMo DCI, as well as to achieve an understanding of how the failure mode is affected by temperature. Numerous other researchers have already reported on the tensile stress-strain behavior and failure modes of HiSiMo DCI including the role of graphite nodules on fracture, and in particular have examined the damage modes that affect fracture at 400 °C where the ductility of the material is severely impaired. For example, see *Sponseller et al.* (1968), *Adewara and Loper* (1975), *Yanagisawa et al.* (1980), *Eldoky and Voigt* (1985), *Wright and Farrell* (1985), *Dong et al.* (1997), *Kobayashi et al.* (1998), *Di Cocco et al.* (2010) and others. However, a holistic review of the activated damage mechanisms is necessary in the current work to relate to observations made under cyclic thermal and mechanical loadings.

Tensile fracture in HiSiMo DCI tends to occur in a ductile manner at low and high temperatures. Examining first the tensile fracture at room temperature in Figure 2.8a, it is apparent that fracture occurs predominantly via cavities that form around the graphite nodules due to fracture of the nodules. This mechanism was studied by *Dong et al.* (1997) via *in situ* SEM observations during tensile deformation of a ductile cast iron alloy. The authors found that matrix plastically deforms via slip lines near the equator of the graphite nodules, even under macroscopically elastic loads. Later, *Di Cocco et al.* (2010) found that the local plastic deformation of the matrix would then cause cracks to initiate within the graphite nodules between the nucleus and the outer shell of the nodule. Under further deformation, this would cause the pole caps of the graphite nodules to detach from the core via an "onion-like peeling" mechanism. This mechanism is observed at room temperature, and a nodule fractured in this manner is shown in Figure 2.8b. Fracture in the remaining material ligaments occurs by microvoid coalescence, as highlighted in Figure 2.8c, resulting in a dimpled appearance of the fracture surface.

No significant intergranular fracture is observed at room temperature. Some small areas of brittle transgranular cleavage are found to be interspersed throughout the ductile transgranular fracture, with an appearance shown in Figure 2.8d.

At intermediate temperatures, the tensile crack grew throughout the fracture surface by a mix of predominantly ductile transgranular (thought some transgranular cleavage is present) and intergranular fracture. These modes are denoted by "TG" and "IG", respectively, in Figure 2.9 for specimen tested at 300 °C, in Figure 2.10 for a specimen tested at 400 °C, and Figure 2.10 for a specimens tested at 500 °C. Intergranular facets were easily observable between regions of ductile transgranular fracture, as shown in Figure 2.9b, Figure 2.10b and Figure 2.10b. Furthermore, chemical analysis performed by energy dispersive spectroscopy (EDS) of the fracture surfaces show the presence of aluminum, manganese and chromium, as well as magnesium. These elements are known to collect in the intergranular space during solidification due to their low melting temperatures. Many shrinkage pores, shown in detail in Figure 2.9c and Figure 2.10c and are also known to form between grains, are present on the fracture surfaces obtained at these temperatures. Intergranular fracture is most prevalent in the specimens tested at 400 and 500 °C and chemical analysis of these fracture surfaces show the highest content of magnesium.

Graphite nodules at 300 and 400 °C show a lesser degree of onion-like peeling than observed at lower or higher temperatures. Instead, graphite nodules at the intermediate temperatures tend to be fractured through the nucleus (or core) of the nodule. A nodule damaged in this manner is shown in Figure 2.9d. This mode of nodule damage was observed by *Di Cocco et al.* (2010) in *in situ* SEM observations of ferritic DCI tested at room temperature at high or low strain rates (1×10^{-2} or $1 \times 10^{-5}\,\mathrm{s}^{-1}$, respectively), or under high stresses. In the present work, it is proposed that the ability of the matrix to accommodate plastic flow was greatly reduced due to the dense distribution of intergranular cracks, resulting in higher stresses locally

and causing fracture in the nucleus of the nodules.

When the temperature is high, at 600 °C or higher, the fracture surface has the appearance of ductile fracture throughout, as shown in Figure 2.11, Figure 2.12 and Figure 2.13 for specimens tested at 600, 700 and 800 °C, respectively. In this case, the fracture of the graphite nodules is not pronounced, though onion-like peeling is evident. The material ligaments then undergo extensive plastic deformation and fail by necking. This results in the severely enlarged appearance of the cavities surrounding the graphite nodules.

Examination of the longitudinal cross-sections in Figure 2.14 confirms the fractographic findings. In particular, the high degree of intergranular cracking is evident when examining the longitudinal cross-sections at 300, 400 and 500 °C in Figure 2.14b, Figure 2.14c and Figure 2.14d, respectively. The intergranular cracks tend to form on a plane that is normal to the direction of the applied load, as shown in Figure 2.15, from the specimen examined at 400 °C. The growth of cavities is clearly reduced at 300 and 400 °C in favor of intergranular cracking, while both cavity growth and intergranular fracture are present at 500 °C. The extent of cavity growth at different temperatures is apparent when examining longitudinal cross-sections through the fracture surfaces of the tested specimens in Figure 2.14. Particularly when the temperature is high, at 600 °C or above, the elongation of cavities around the nodules is severe and can be several times greater than the diameter of the nodule.

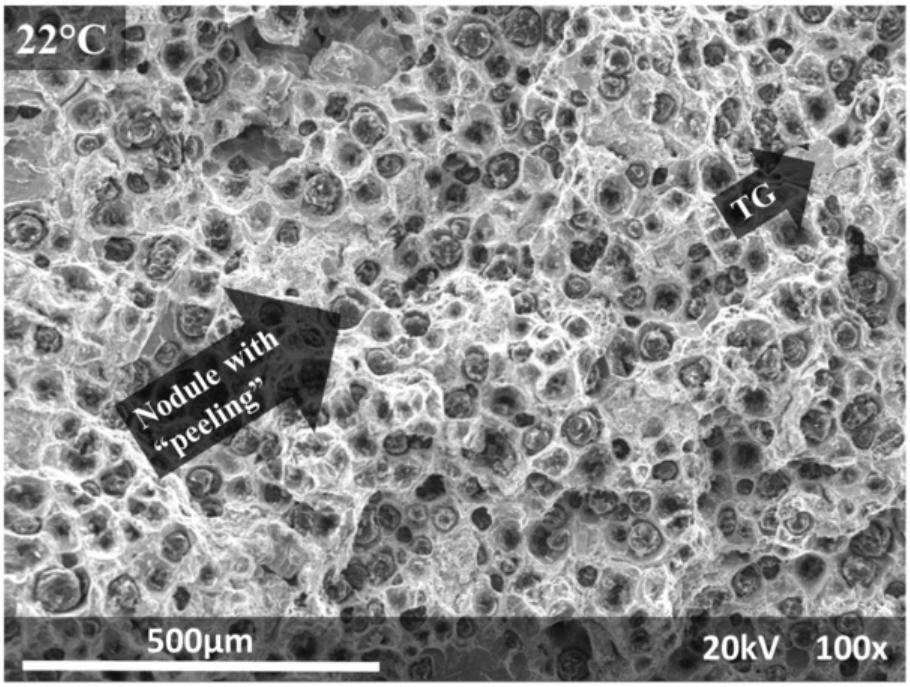

(a)

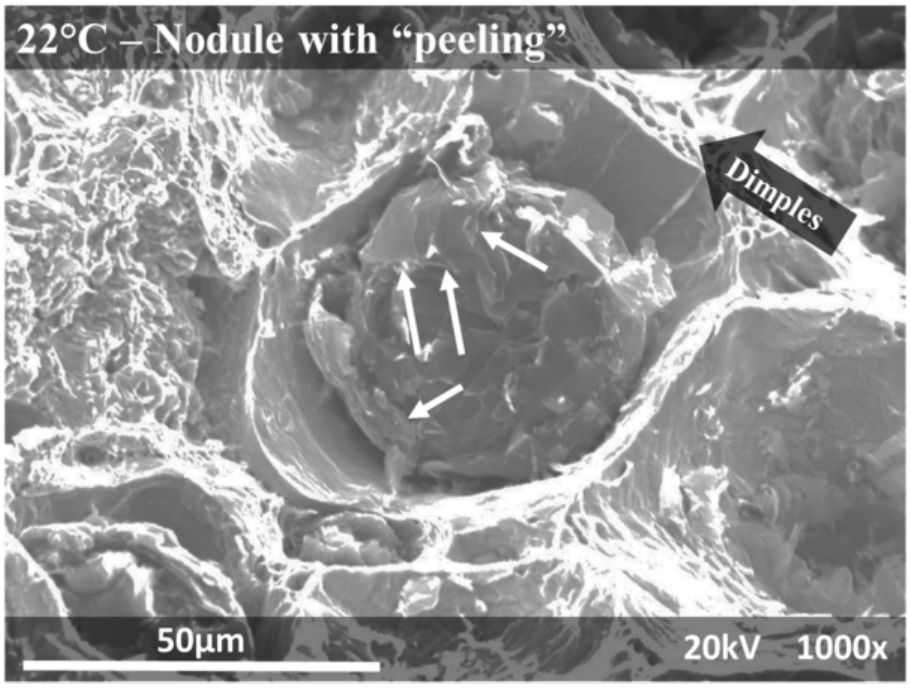

(b)

Figure 2.8: SEM image of (a) the fracture surface in a specimen tested under quasi-static conditions at 22 °C featuring (b) nodules damaged by onion-like peeling. Continued on next page, SEM image of (c) dimples caused by microvoid coalescence and (d) brittle transgranular cleavage.

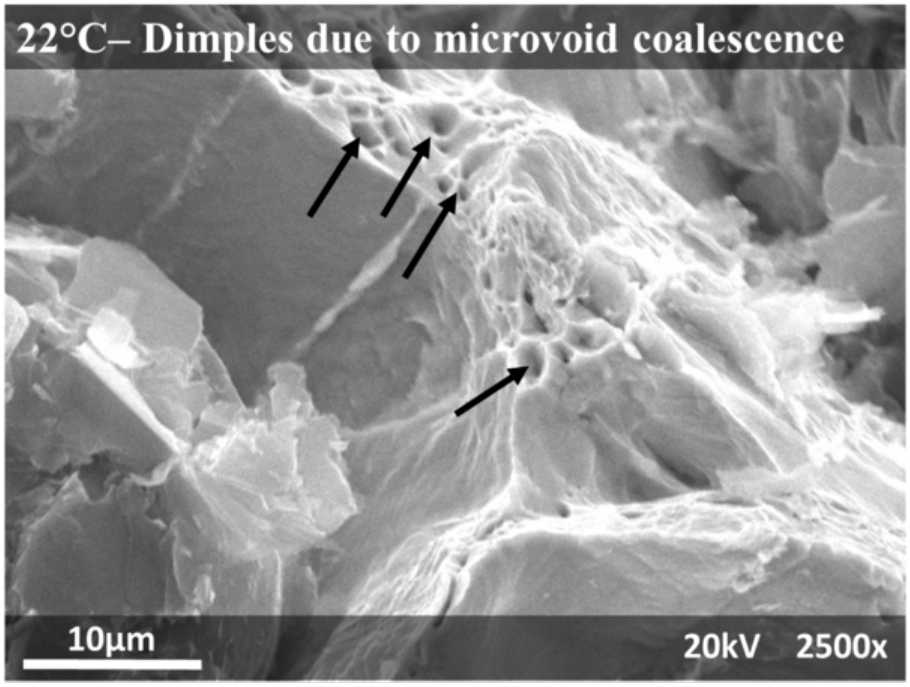

(c)

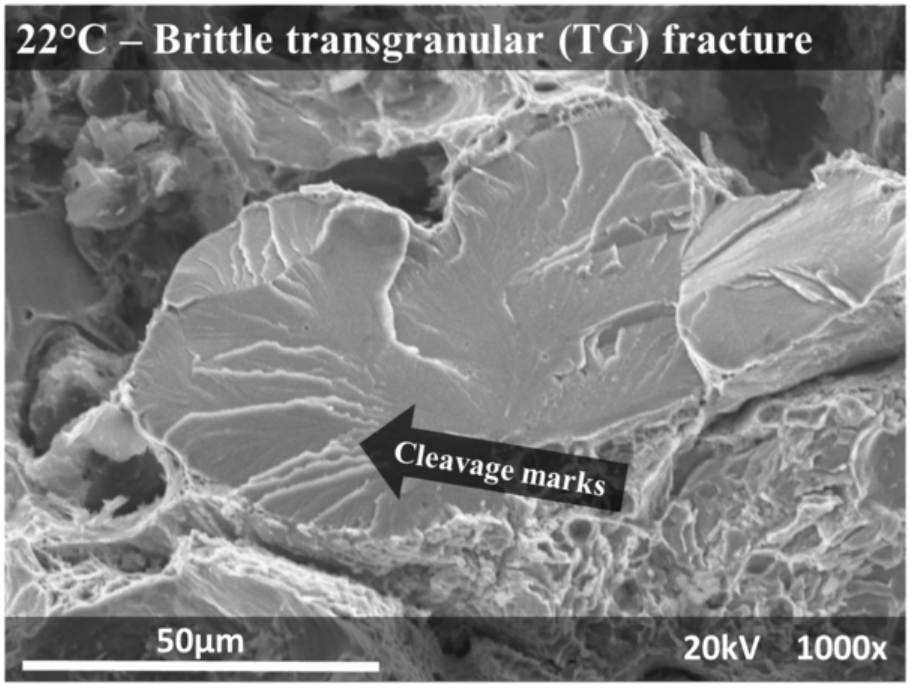

(d)

Figure 2.8: Continued from previous page.

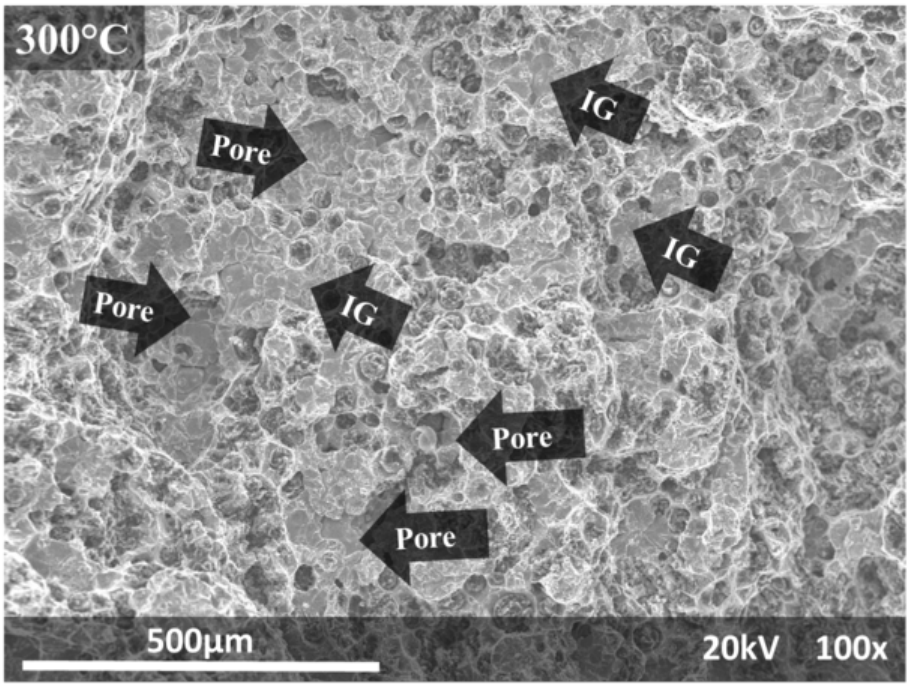

(a)

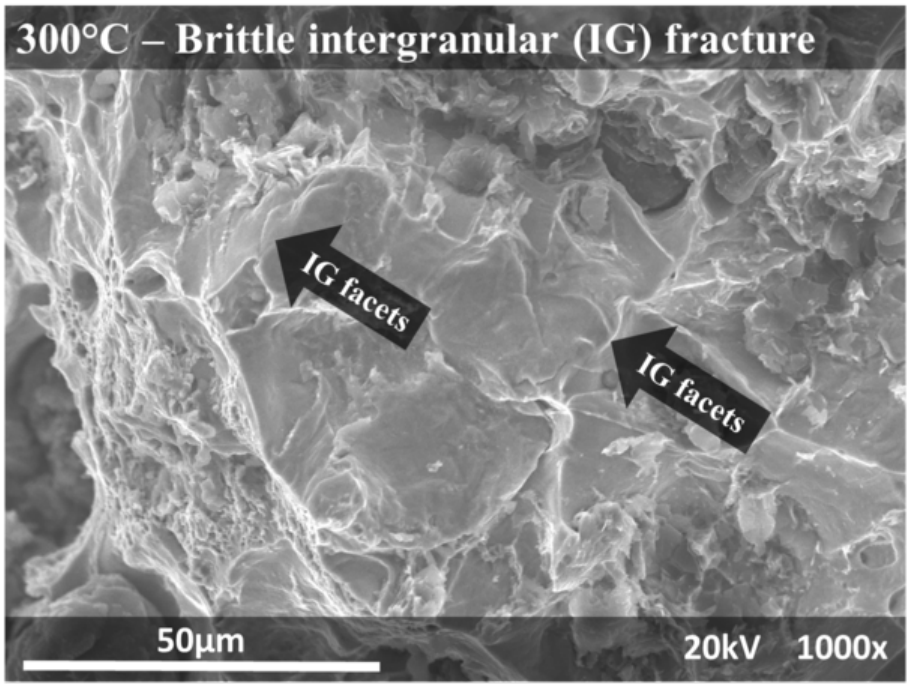

(b)

Figure 2.9: SEM images of (a) the fracture surface in a specimen tested under quasi-static conditions at 300 °C and (b) brittle intergranular fracture. Continued on next page, SEM image of (c) shrinkage pore and (d) a nodule fractured through the nucleus (outlined).

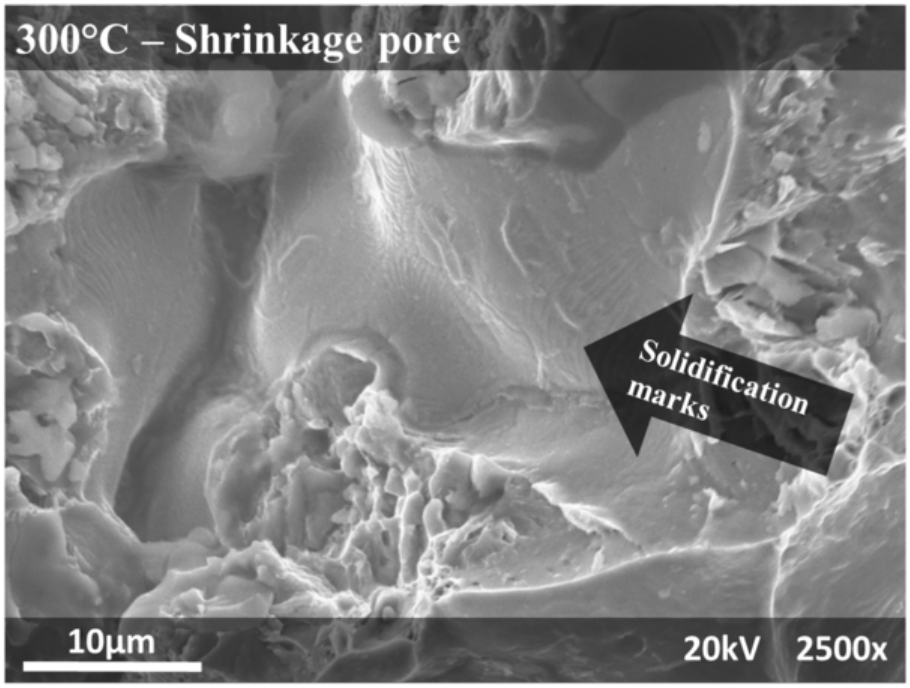

(c)

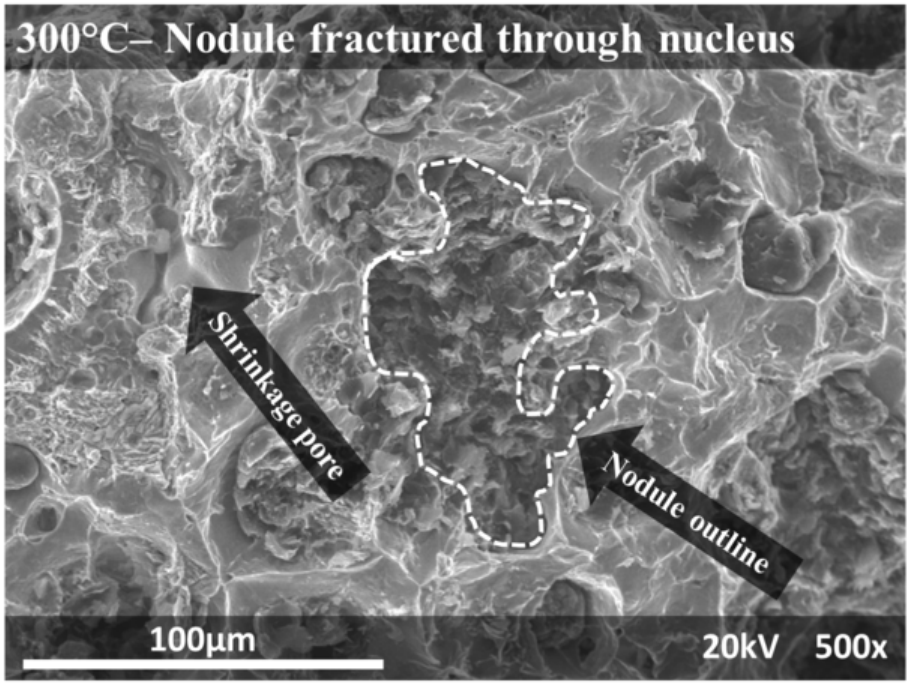

(d)

Figure 2.9: Continued from previous page.

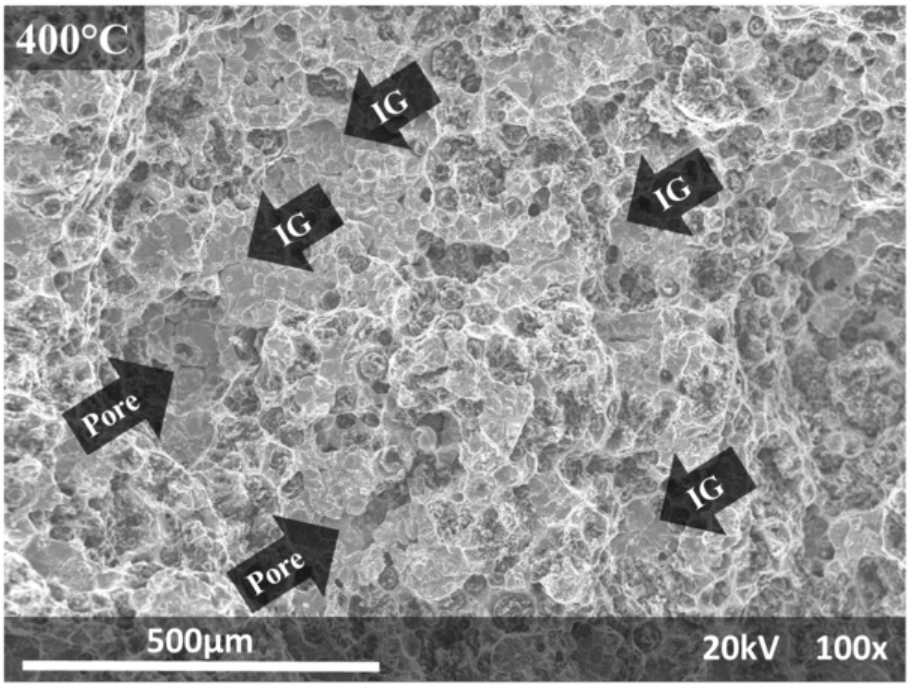

(a)

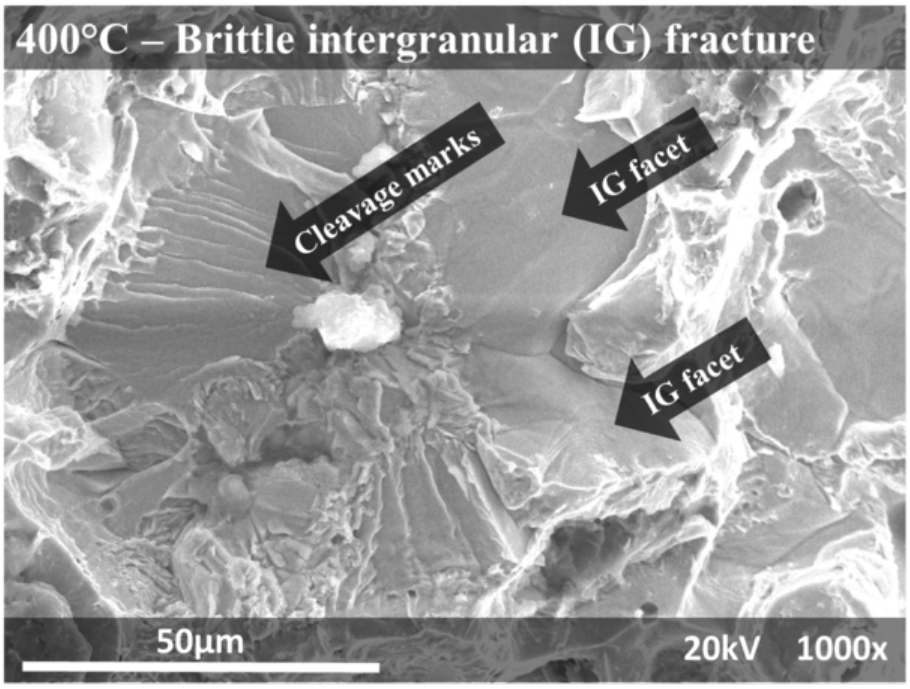

(b)

Figure 2.10: SEM images of (a) the fracture surface in a specimen tested under quasi-static conditions at 400 °C and (b) brittle intergranular fracture. Continued on next page, SEM image of (c) shrinkage pore identified by solidification marks.

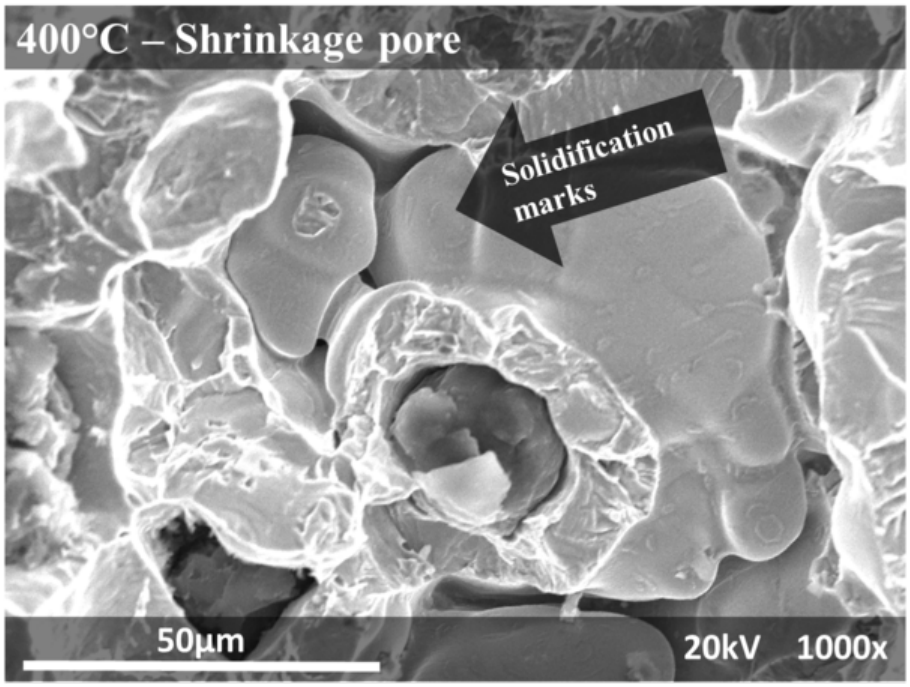

(c)

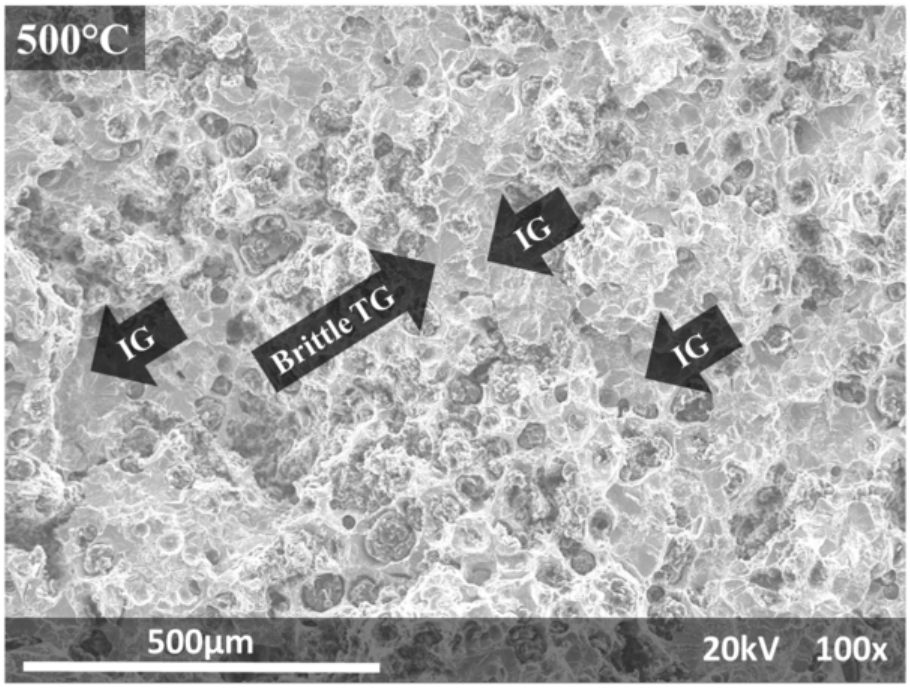

(a)

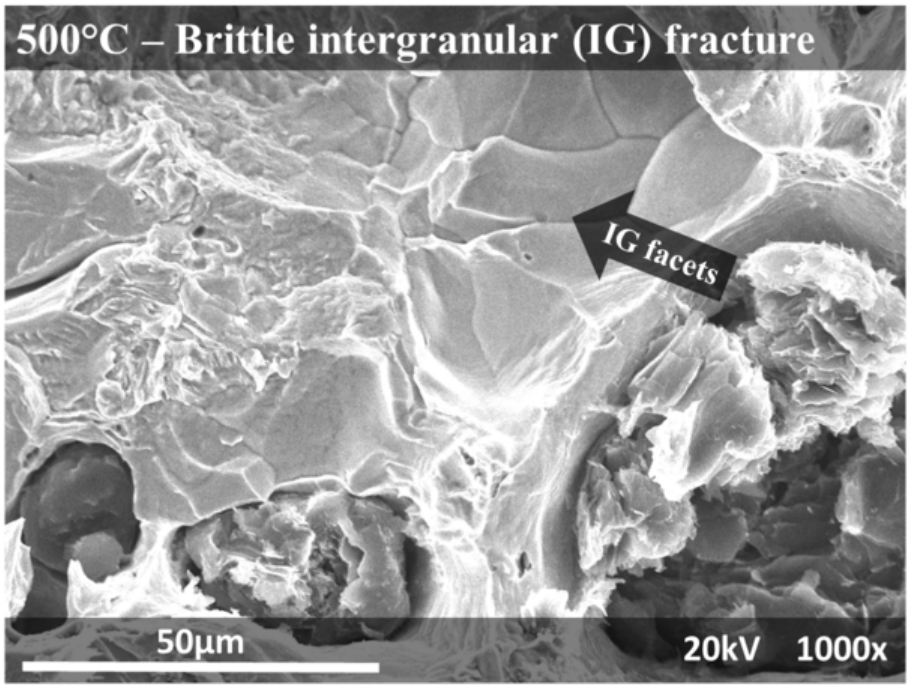

(b)

Figure 2.10: SEM images of (a) the fracture surface in a specimen tested under quasi-static conditions at 500 °C and (b) intergranular fracture.

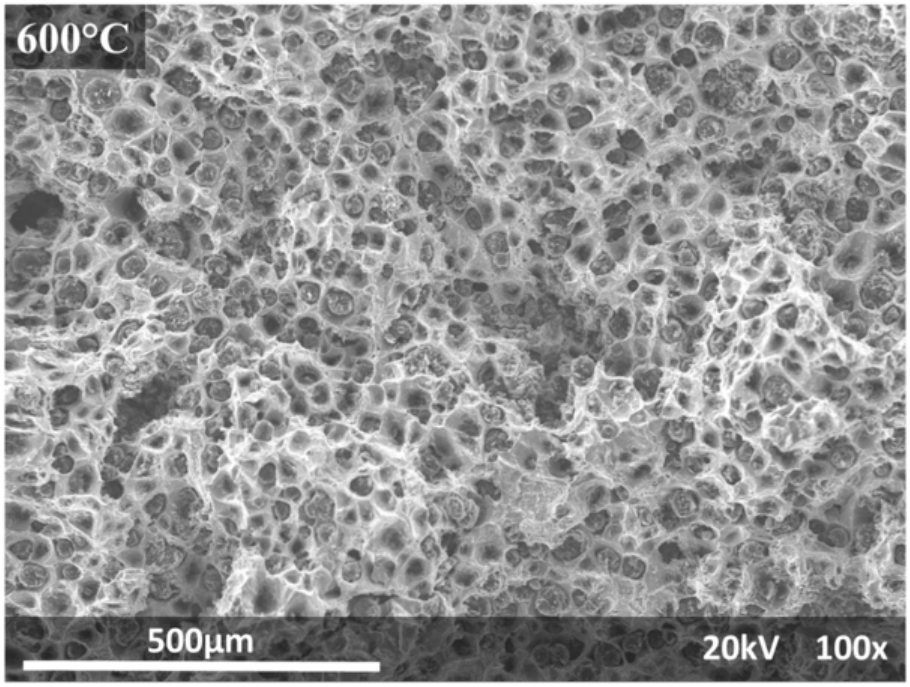

Figure 2.11: SEM images of the fracture surface in a specimen tested under quasi-static conditions at 600 °C where failure occurred by ductile necking of the material ligaments between the graphite nodules.

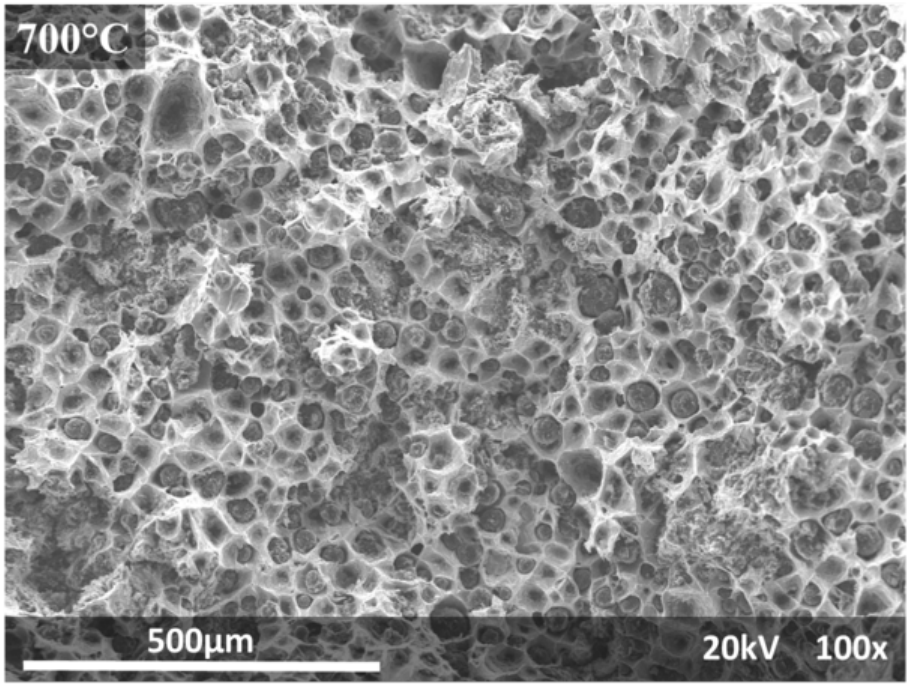

Figure 2.12: SEM images of the fracture surface in a specimen tested under quasi-static conditions at 700 °C where failure occurred by ductile necking of the material ligaments between the graphite nodules.

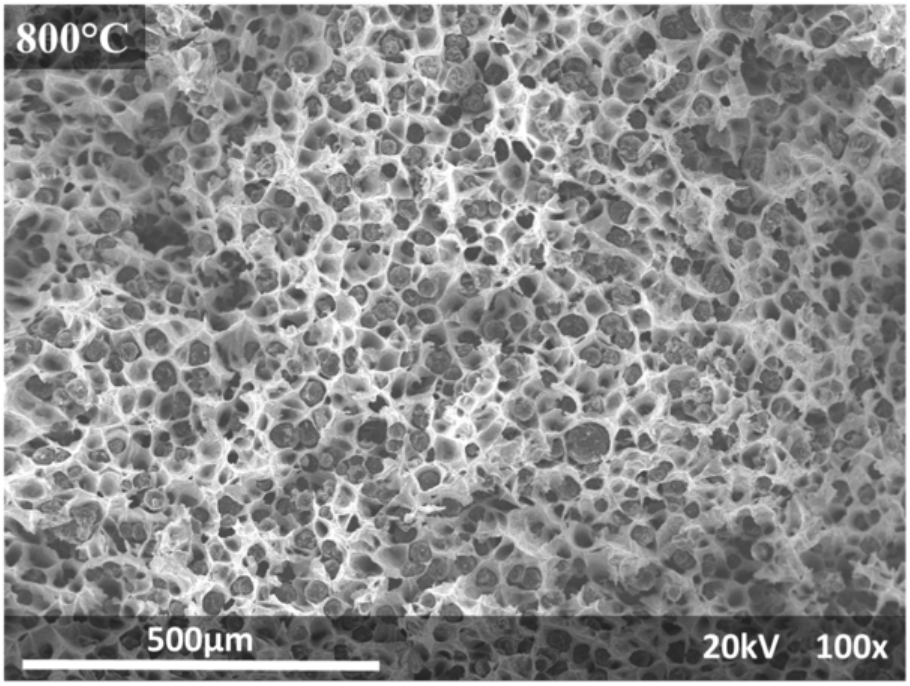

Figure 2.13: SEM images of (a) the fracture surface in a specimen tested under quasi-static conditions at 800 °C where failure occurred by ductile necking of the material ligaments between the graphite nodules.

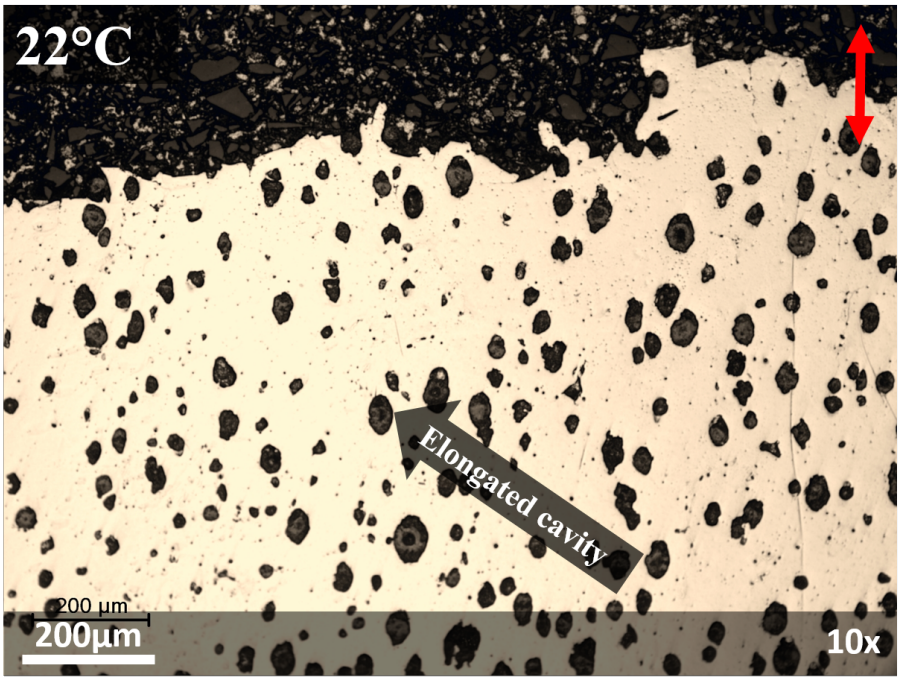

(a)

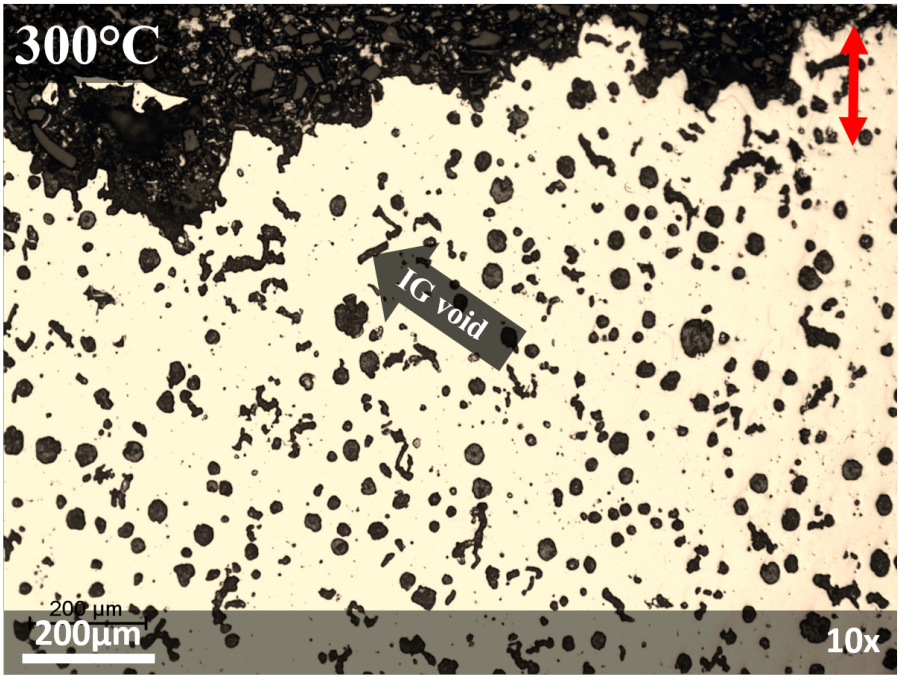

(b)

Figure 2.14: Optical micrographs of a longitudinal cross-section through the tensile fracture surfaces obtained from quasi-static tests at (a) room temperature and (b) 300 °C. Continued on next page, (c) 400 °C, (d) 500 °C, (e) 600 °C, (f) 700 °C and (g) 800 °C. Arrows show loading direction.

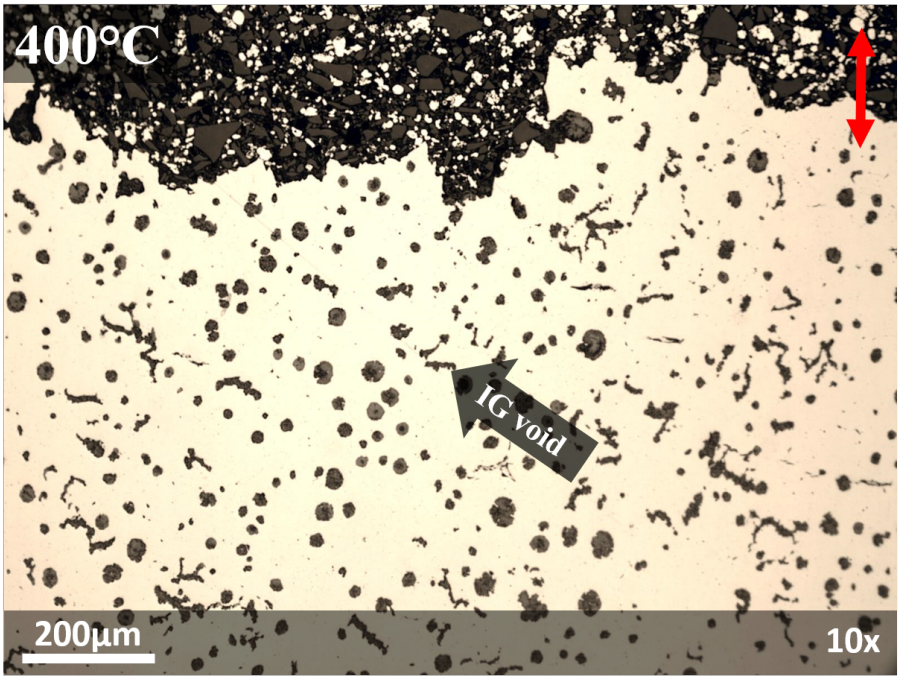

(c)

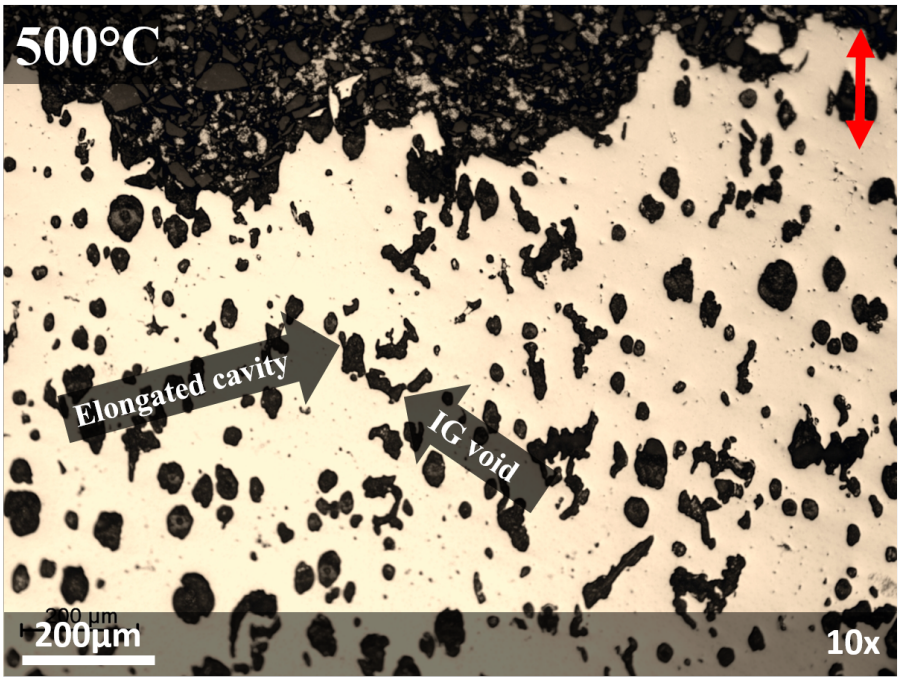

(d)

Figure 2.14: Continued from previous page.

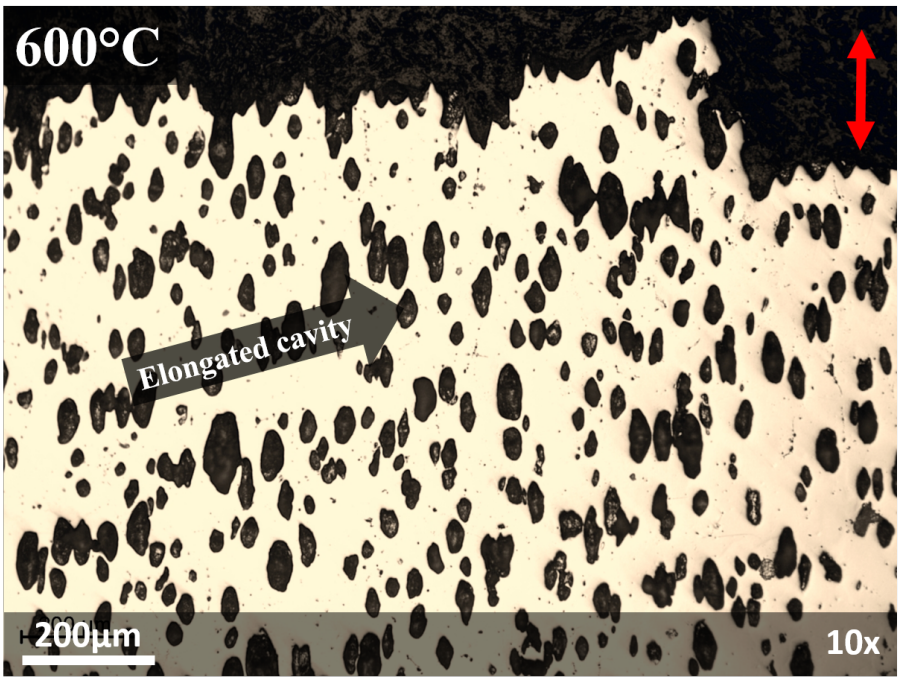

(e)

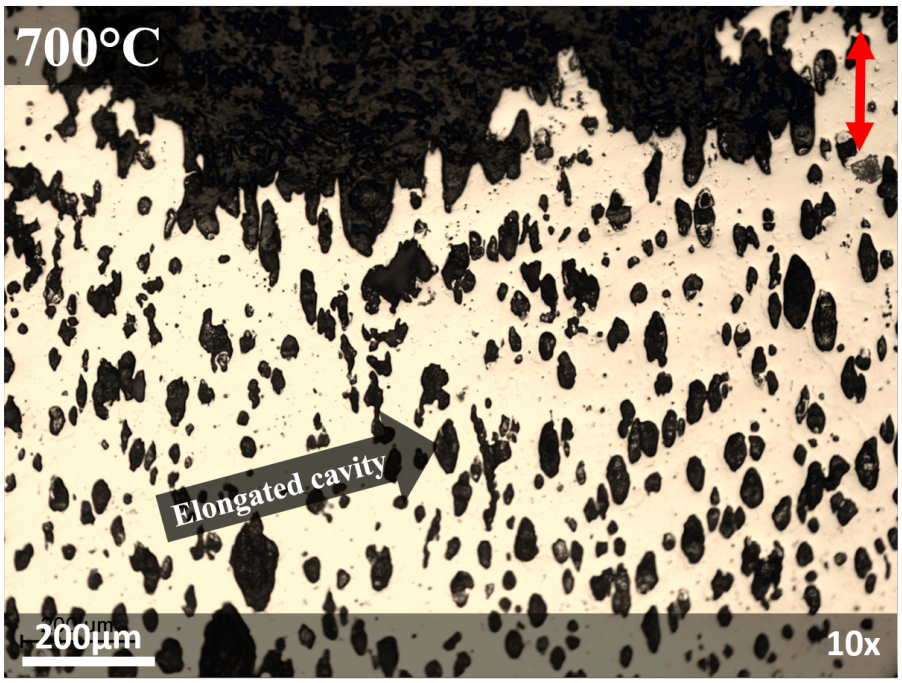

(f)

Figure 2.14: Continued from previous page.

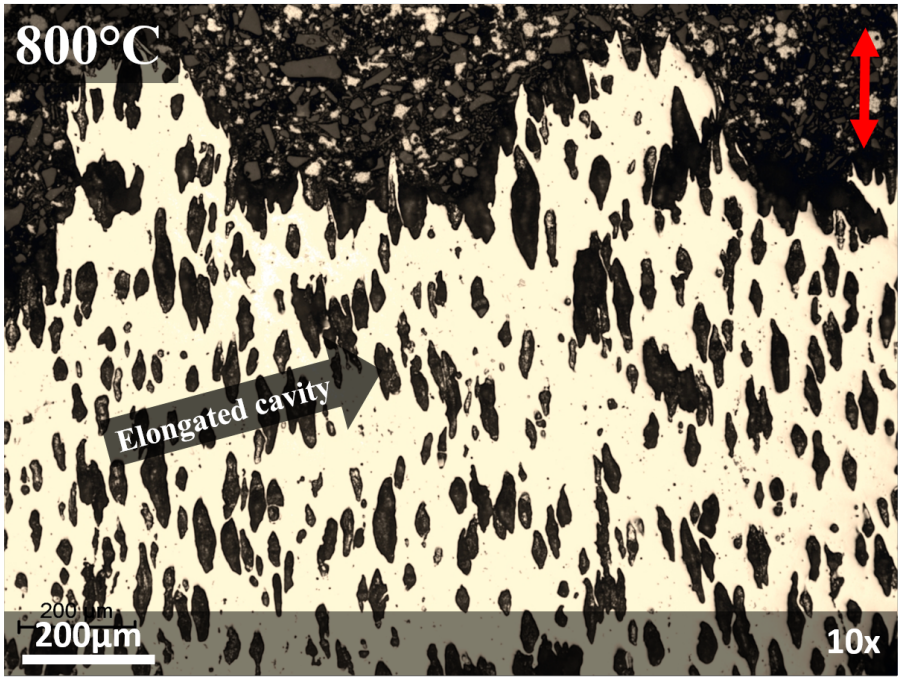

(g)

Figure 2.14: Continued from previous page.

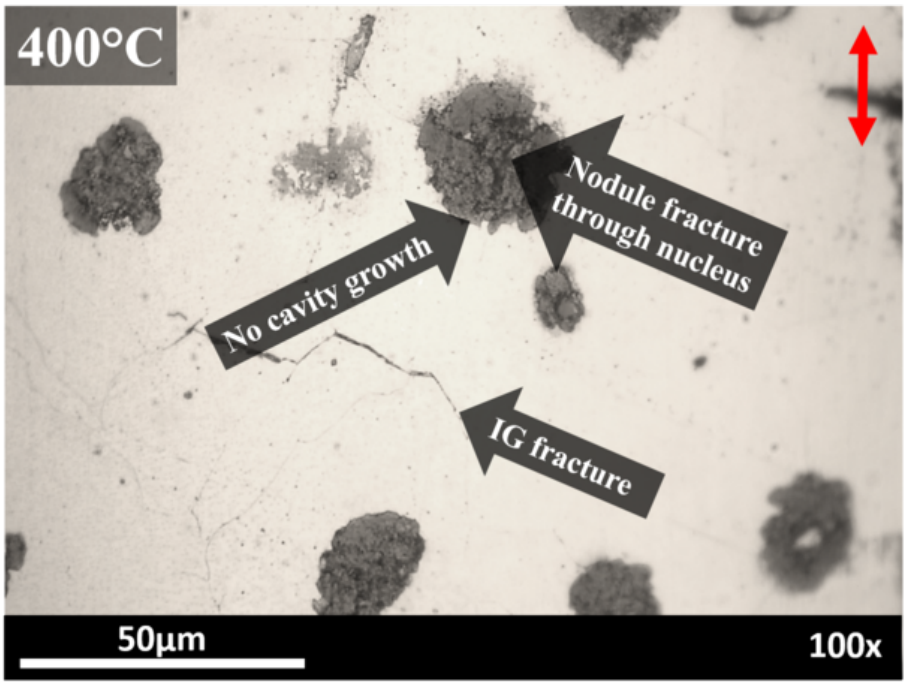

Figure 2.15: Magnified view of intergranular fracture in the cross-section of a specimen tested under quasi-static conditions at 400 °C. Specimen was lightly etched with 2 % Nital for 10 s. Arrow shows loading direction.

2.3.3 Discussion

The macroscopic, phenomenological behavior of HiSiMo DCI under quasi-static tensile loading can be correlated to microstructural features in the crack path. In general, the strength will decrease as the temperature increases due to increased plastic flow of the ferritic matrix upon deformation. Similarly, when the plastic flow of the matrix is inhibited due to the energetically-favorable, temperature-dependent fracture of magnesium-rich grain boundaries, the strength values tend to remain fairly high while the ductility suffers a dramatic reduction. Microscopically, the ductile mode of fracture in these cases is offset by the lower-energy processes of transgranular cleavage and brittle intergranular fracture. This latter effect is pronounced at temperatures near 400 °C.

2.3.3.1 Intermediate Temperature Embrittlement of HiSiMo DCI

The embrittlement phenomenon has been observed in ferritic DCI at intermediate temperatures nearly since the introduction of the alloy (*Fitzgeorge and Pope*, 1953). A similar phenomenon has also been observed at intermediate temperatures in copper and copper-base alloys, nickel and nickel-base alloys, aluminum, lead and tin alloys and some stainless steels that contain some low-melting temperature impurity element which causes an embrittlement at the grain boundaries (*Arkoosh and Fiore*, 1972; *Roth et al.*, 1980; *Sandchez-Medina et al.*, 1981; *Suzuki et al.*, 1981; *Bouchaud et al.*, 1991; *Laporte and Mortensen*, 2009). The impurity elements may or may not be intentionally added to the alloy melt, and the loss of ductility corresponds to either liquid metal embrittlement or migration of solid inclusions to the grain boundaries.

Following the earliest of these works, *Yanagisawa et al.* (1980) found that the brittle behavior of ferritic DCI near 400 °C was accompanied by a high degree of intergranular fracture, and the embrittlement phenomenon was dependent on both temperature and strain rate. *Wright and Farrell* (1985) later conducted a detailed

study to fully characterize the embrittled fracture behavior under tensile and low cycle fatigue loading conditions for twenty-six different alloys of DCI with varying contents of silicon, pearlite, and different nodule shapes. The authors conducted tensile tests at strain rates between $8.3 \times 10^{-5}\,\mathrm{s}^{-1}$ and $2 \times 10^{-2}\,\mathrm{s}^{-1}$, at temperature ranging from ambient up to 734 °C in air, and at 425 °C in a vacuum. It was found that reducing levels of magnesium and/or sulfur could greatly reduce the severity of the embrittlement phenomenon, so long as sufficient magnesium was present to fully inoculate the alloy (as poorly formed nodules can also reduce the dutility of the alloy). Intergranular fracture was found to be prevalent at low levels of ductility near 400 °C, and the fracture surface was found to contain significant quantities of magnesium and magnesium oxide. *Kobayashi et al.* (1998) found that the temperature of embrittlement varies most signficantly with the changes in the content of magnesium, sulfur and phosphorus, and is additionally affected by strain rate. The temperature of minimum ductility falls between about 350 and 450 °C (*Wright and Farrell*, 1985; *Kobayashi et al.*, 1998).

Magnesium serves as a powerful inoculant for cast iron and is extensively used in the production of nodular cast iron to create the spheroidal form of graphite that improves ductility and toughness in cast iron (*Norman et al.*, 1949). Additionally, magnesium is commonly used in iron-base alloys to remove impurities, like sulfur, that can have a deleterious effect on the toughness, ductility, weldability and corrosion resistance of the alloy. The combined impurities then float to the top of the melt as slag and can be removed to improve the quality of the alloy (*Chute*, 1907). However, magnesium is fairly insoluble in iron and, upon solidification of an ferrous alloy, any uncombined magnesium tends to segregate to the grain boundaries as the last liquid to solidify, carrying with it some quantity of the impurities it has scavenged. The amount of impurity remaining in the melt would depend on the alloy content, quantity and timing of magnesium additions, quality of the pig iron, and time in the melt. The

presence of impurity elements at the grain boundaries, particularly those with low melting or vaporization temperatures, can contribute signficantly to the ease of grain boundary fracture *Arkoosh and Fiore* (1972); *Roth et al.* (1980); *Sandchez-Medina et al.* (1981); *Suzuki et al.* (1981); *Wright and Farrell* (1985); *Bouchaud et al.* (1991); *Laporte and Mortensen* (2009)

2.3.3.2 Thoughts on Reducing Embrittlement by Changing Alloy Chemistry

Given that HiSiMo is the most commonly used material for exhaust manifolds in the United States, it would be worthwhile to explore changes in chemistry which could reduce the severity of the ductility trough and allow for a greater focus on reducing weight or cost when optimizing a design. *Kobayashi et al.* (1998) studied the tensile and bending behavior of 26 alloys with similar silicon content but varying contents of manganese, magnesium and phosphorus. The authors proposed that sufficient phosphorus present in a ferritic spheroidal cast iron with silicon content ranging from 3.5 to 4.2 % could provide relative immunity to the embrittlement phenomenon. The greatest loss of ductility occurred in alloys containing a ratio of magnesium to phosphorus (Mg/P) exceeding about 1.5 when comparing tests at the same strain rate. By careful control of minute additions of phosphorus, the effect of 400 °C embrittlement of sulfur could be greatly reduced.

Phosphorus is known to retard the precipitation of sulfides and can provide significant solid-solution strengthening, improved machinability and corrosion resistance to ferritic structures. However, in ductile cast iron alloys, it can also promote shrinkage porosity, and reduce ductility and tensile strength due to embrittlement caused by the segregation of iron phosphide to the grain boundaries (*Angus*, 1960; *Minkoff*, 1983). In ductile iron, such as HiSiMo, phosphorus has a strong embrittling effect at levels as low as 0.02 % and is typically considered an impurity element (*Ductile*

Iron Society, 1998). Thus, efforts to control the effect of sulfur embrittlement of a HiSiMo alloy through changes in the alloy chemistry should be conducted with strict consideration of both the benefit and risk of changes in the chemistry.

Furthermore, no studies have been found in the literature where changes in chemistry intended to reduce the effect of sulfur embrittlement have included the high temperature fatigue or thermomechanical fatigue performance of the alloy. It is recommended that efforts to reduce the severity of 400 °C embrittlement through alloy chemistry also include a comprehensive study of all the relevant performance metrics for the exhaust manifold application.

2.3.4 Summary of the Tensile Behavior and Failure Modes of HiSiMo DCI

A thorough examination of the tensile behavior of HiSiMo DCI was conducted to learn the relevant damage modes which can influence the constitutive behavior of the material at elevated temperatures. The key findings of the tensile characterization of the HiSiMo DCI considered in the present study are summarized below:

1. Young's modulus, proof strength and tensile strength decrease with increasing temperature,
2. The graphite nodules tend to initiate a ductile mode of fracture, provided the ferritic matrix can accommodate sufficient plastic flow,
3. The ability of the matrix to macroscopically undergo plastic flow is inhibited near 400 °C due to the embrittlement done to the grain boundaries by free sulfur as it evaporates,
4. Consequently, elongation and reduction in area undergo a minimum at 400 °C which is recovered at higher temperatures,
5. Finally, the matrix tends to fracture via cavity growth and microvoid coalescence at low temperatures, by brittle intergranular fracture at intermediate temperatures, and by severe plastic deformation of the matrix at high temperatures.

From these observations, it is clear that the energetically-favorable mode of fracture in HiSiMo DCI changes dramatically with temperature. Particularly at inter-

mediate temperatures, the tensile fracture of HiSiMo DCI occurs in a brittle manner at low levels of strain. Thus, the ability of the material to dissipate strain energy is inhibited at intermediate temperatures.

2.4 Low Cycle Fatigue Characterization

The HiSiMo DCI considered in this study was additionally characterized under low cycle fatigue conditions for temperatures ranging from ambient up to 800 °C. The test procedures and results are described in the following sections, along with fractography to characterize the relevant damage processes under these loading conditions.

2.4.1 Test Procedure

Isothermal LCF tests were conducted on specimens of HiSiMo DCI to determine the low cycle fatigue behavior and strain-life (ε-N) relationship at room temperature, 200, 400, 500, 600, 720 and 800 °C. A limited number of cyclic creep tests were conducted at 600 °C. Additionally, tests at 800 °C were conducted with different strain rates, and also with a tensile or compressive hold times. A total of 69 specimens were tested to failure under isothermal fatigue conditions. Specimens were created with a geometry according to *ASTM E606* (2004) for strain-controlled fatigue testing. Specimens were machined from as-cast bars using a lathe. Specimens for room temperature tests were left with smooth shoulders, while specimens for elevated temperature tests were cut with threads in the shoulder section to accommodate the high-temperature grips. After machining, specimens were polished longitudinally with low-stress grinding to a surface roughness of Ra16. The diameter of each specimen was measured with a non-contact method at three locations in the reduced section of the specimen, and the average diameter was used for the calculation of stresses. The diameter measurements range from 7.63 to 7.65 mm.

LCF tests were conducted at Westmoreland Testing and Research Center in

Youngstown, PA on a servo-hydraulic test frame outfitted with a 89 kN (20,000 lb) load cell and water-cooled grips (*Jones*, 2014). Strain was measured via a water-cooled high temperature extensometer held in place against the specimen with a spring-loaded arm. Strain and temperature were continually monitored and controlled through in-house software. Heating for elevated-temperature LCF tests was achieved through use of a two-zone clam-shell resistance furnace for tests conducted up to and including 600 °C (*Jones*, 2014). Induction heating was used for tests at 720 and 800 °C. A temperature profile for each heating method was created from a sacrificial specimen with multiple thermocouples welded within the gauge length and at the radii to ensure a uniform temperature was achieved in the gauge length. The temperature in the specimen radius was correlated to the temperature in the gauge length. Temperature was monitored during testing via a single reference thermocouple welded to the specimen radius.

The in-house software was used to gradually bring the specimen to the test temperature. Specimens were soaked at the test temperature for one hour to ensure a homogeneous temperature (*Jones*, 2014). Fully reversed tests were conducted with a triangular waveform at a constant strain rate of $5 \times 10^{-3}\,\mathrm{s}^{-1}$. The strain amplitude was gradually increased within the first 10-20 cycles until the target value was reached. Fatigue life was determined by a 50 % drop in maximum load from the stabilized value; tests were discontinued at 2×10^5 cycles. A minimum of four specimens were tested for each ε-N curve.

Upon completion of each test, the specimen was allowed to cool to room temperature by natural convection. Specimens were carefully packed individually in with the shoulder ends facing each other to protect the fracture surfaces, and were shipped to Ford Motor Company in Dearborn, MI for further examination. The fracture surfaces were inspected with optical and scanning electron microscopy (SEM). SEM was performed with a spot size of 50 and acceleration voltage of 20 kV. Energy dis-

persive spectroscopy (EDS) was performed on the fracture surfaces to determine the chemical composition present in the crack path. EDS measurements were taken in topographically-similar regions of each fracture surface and are reported as values averaged from at least six measurements. EDS was conducted at a working distance of 10 mm and an acceleration voltage of 20 kV with a detector at an angle of 8° from the longitudinal axis of the sample.

2.4.2 Results

2.4.2.1 Strain-Life Behavior

The HiSiMo alloy was found to be cyclically stable at all tested temperatures once the target strain amplitude was achieved (within the first 10-20 cycles), as shown in Figure 2.16. The strain-life (ε-N) plot is shown in Figure 2.17a for LCF tests at all temperatures. The curves shown in the Figure represent the average behavior for tests conducted at each temperature. The ε-N behavior is similar for tests conducted at room temperature and 200 °C. The ε-N curve has the same slope for tests conducted at 400 and 500 °C as the lower test temperatures; however, the fatigue life is reduced by almost an order of magnitude at these higher temperatures. As the test temperature increases, the slope of the ε-N curve increases. Tests at 720 and 800 °C result in similar ε-N curves.

Similar results have been reported by *Yanagisawa et al.* (1980), who examined the rotating bending fatigue strength of ferritic DCI at elevated temperatures, and found that a sharp decrease in fatigue strength occurred at 400 to 500 °C. More recently, *Wu et al.* (2013) showed that the LCF performance of HiSiMo DCI is reduced at 400 °C when compared to other temperatures.

When the test temperature is increased to 600 °C, the slope of the ε-N curve is steeper than at lower temperatures. At high strain ranges at 600 °C, the fatigue life is similar to that of the room temperature tests, but at low strain ranges, fatigue life is

significantly reduced. The cross-over behavior of HiSiMo DCI is further accentuated when the test temperature is higher, at 720 or 800 °C. Here, the long life is more significantly reduced from that observed at the lower temperatures, while the fatigue life at high strain ranges is nearly identical to that observed at room temperature. Thus, increasing the test temperature does not strictly decrease life, and the strain-life curves appear to converge at high values of strain.

For the same applied mechanical strain range, the magnitude of the inelastic component of strain generally increases as the temperature increases, except at 400 °C. The Coffin-Manson plots, showing the relationship between inelastic strain amplitude and fatigue life, are shown in Figure 2.17b. Especially at high levels of inelastic strain, the life at 400 °C is significantly shorter than that at any other temperature. The curve for tests conducted at 500 °C falls between that of the room temperature and 200 °C tests, rather than between the curves for 200 and 600 °C.

In general, the slope of the inelastic strain-life curve decreases with increasing temperature, indicating that the measured life becomes increasingly sensitive to changes in the inelastic strain amplitude. *Coffin* (1973) observed a "convergence behavior" for strain-controlled tests conducted at elevated temperatures, where the inelastic strain-life curves converge to a point that is roughly bounded between the curves at low and high temperatures. This behavior is observed in the HiSiMo DCI, except for the curve at 400 °C. The slope of this curve is similar to that at high temperatures, indicating that life is less sensitive to changes in the inelastic strain. The same trend in convergence behavior was observed by *Charkaluk and Constantinescu* (2000) and *Wu et al.* (2013). This observation suggests that damage is occurring by a different mechanism at 400 °C that is not predominant at the other tested temperatures.

In an effort to better understand the strain-life behavior of HiSiMo DCI, the strain-life parameters were calculated at each temperature. The strain-life equation for fatigue life is the combination of the Basquin equation for stress-controlled fatigue

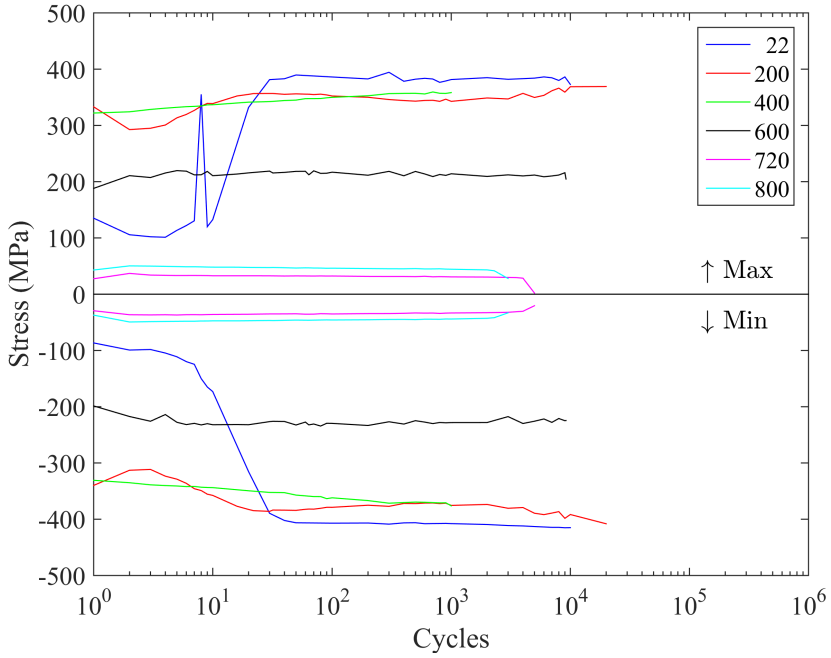

Figure 2.16: Evolution of the maximum and minimum stress in low cycle fatigue with a strain amplitude of approximately 0.005 from room temperature up to 800 °C.

life (*Basquin*, 1910) and the Coffin-Manson relation for strain-controlled fatigue life (*Manson*, 1953; *Coffin*, 1954). The strain-life equation is given by

$$\frac{\Delta\varepsilon_{mech}}{2} = \frac{\sigma'_f}{E}(2N_f)^b + \varepsilon'_f(2N_f)^c \tag{2.1}$$

where $\Delta\varepsilon_{mech}$ is the mechanical strain range, σ'_f is the fatigue strength coefficient, E is the Young's modulus, ε'_f is the fatigue ductility coefficient, b is the fatigue strength exponent, and c is the fatigue ductility exponent. The fitted parameters are reported in Table 2.3. The fatigue strength coefficient (σ'_f) is shown to undergo a slight increase as temperature increases from 200 to 500 °C, and then decrease with further increases in temperature. The fatigue ductility coefficient (ε'_f) increases with increasing temperature, except for a severe decrease at 400 °C. The fitted room temperature values of b and c fall within the typical ranges for steel alloys, which are -0.05 to -0.25, and -0.2 to -1.2, respectively (*Basan et al.*, 2011).

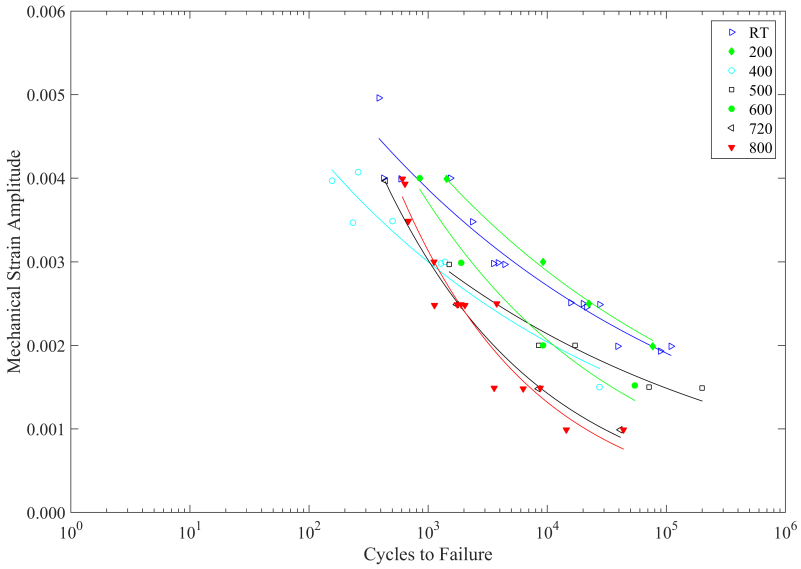

(a)

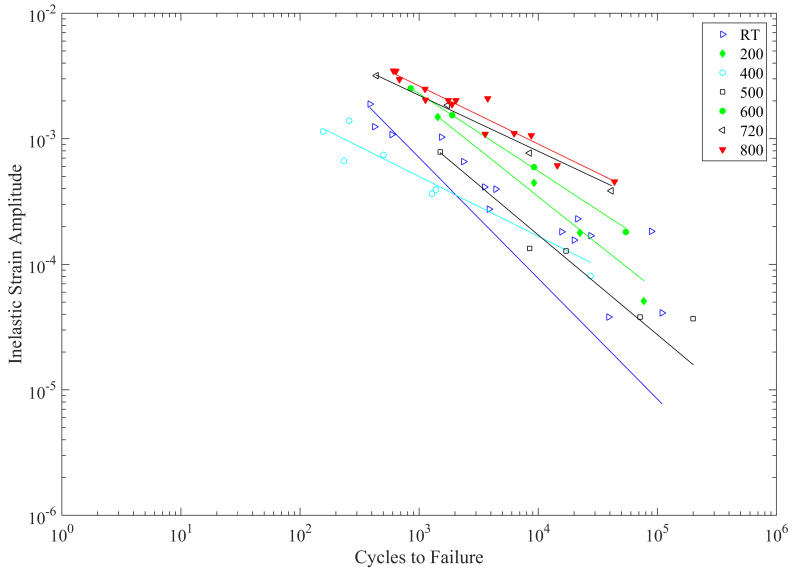

(b)

Figure 2.17: (a) Strain-life and (b) inelastic strain-life curves for low cycle fatigue tests conducted from room temperature up to 800 °C at a rate of $5 \times 10^{-3}\,\mathrm{s}^{-1}$ for HiSiMo DCI.

Table 2.3: The strain-life (ε-N) parameters resulting from LCF tests at a strain rate of $5 \times 10^{-3}\,\mathrm{s}^{-1}$.

Temp.(°C)	$\boldsymbol{\sigma'_f}$	$\boldsymbol{\varepsilon'_f}$	$\boldsymbol{b}$	$\boldsymbol{c}$
22	887	0.162	-0.083	-0.761
200	819	1.418	-0.081	-0.932
400	906	0.088	-0.126	-0.817
500	713	0.151	-0.099	-0.763
600	266	0.195	-0.035	-0.645
720	130	0.062	-0.059	-0.489
800	51	0.076	-0.024	-0.491

2.4.2.2 Observations of Fractured Specimens

To gain an understanding of the complex micromechanical damage processes which take place during the low cycle fatigue damage of HiSiMo DCI, fractography was performed on the tested specimens. Specimens were examined from tests conducted from room temperature up to 800 °C. Furthermore, specimens from both a high strain range and a low strain range were examined for each test temperature to explain the differences in damage mechanisms which cause the cross-over behavior of the strain-life curves. The fracture surfaces were carefully compared to determine differences in the damage mechanisms that might explain the changes in the fatigue strength and ductility as the test temperature changes. A summary of the examined specimens is provided in Table 2.4.

Each specimen tested at a low strain range features a semi-circular region in which the primary mode of damage was advanced in a cyclical manner due to the fatigue loading. These regions are evident in optical micrographs of the fracture surfaces in Figure 2.18. At room temperature and 200 °C, the fatigue region is dominated by the propagation of one primary fatigue crack. At 400 °C and above, multiple initiation sites were found. In the images, the dashed white lines denote the border between the fatigue region(s) and the region of final fracture.

Table 2.4: A list of the specimens examined to determine the damage mechanisms in LCF of HiSiMo DCI.

Specimen No.	**Temp. (°C)**	**Strain**	$\mathbf{N_f}$
13-0201	22	0.0025	27584
13-0199	22	0.0039	1539
13-0210	200	0.0020	77025
13-0207	200	0.0039	1430
13-0214	400	0.0015	27507
13-0211	400	0.0040	156
13-0218	600	0.0015	54422
13-0215	600	0.0040	851
13-0226	720	0.0015	16847
13-0231	720	0.0040	437
13-0221	800	0.0015	3581
13-0219	800	0.0040	640

At a low strain range, fracture tended to initiate at shrinkage pores that intersected the specimen surface. For specimens tested at room temperature, 200, 400 and 600 °C, these regions are shown in Figure 2.19a, Figure 2.20a, Figure 2.18c and Figure 2.18d, respectively. Solidification marks are present which confirm that these features are shrinkage pores, as exemplified in Figure 2.20b and Figure 2.21b. Chemical analysis performed by EDS at the initiation sites for specimens tested up to 600 °C revealed magnesium, molybdenum, aluminum and copper, all of which are expected to be present at the shrinkage pores. Specimens tested at 720 and 800 °C were significantly oxidized at the region of crack initiation, as evident in Figure 2.23a and Figure 2.24, respectively, and the fracture surfaces could not be analyzed by EDS.

The fatigue crack propagated in a predominantly transgranular manner at room temperature and 200 °C. The appearance of the fatigue fracture surfaces are shown in Figure 2.19b and Figure 2.20c, respectively. At 400 °C, damage occurred mainly by intergranular fracture. Intergranular facets, such as those shown in Figure 2.21c

are throughout the region of fatigue crack growth, and shrinkage proes are prevalent on the fracture surface. Chemical analysis conducted via EDS showed a high content of magnesium on the fracture surface at 400 °C, but none at lower or higher temperatures. At 600 °C and higher, significant oxidation was present which obscured the features of the fracture surface.

Nodules in the fatigue region are typically damaged by a combination of onion-like peeling and fracture in the nodule nucleus. These mechanisms were described in detail by *Di Cocco et al.* (2012), who performed *in situ* SEM observations of room temperature fatigue crack propagation in a ferritic DCI. The extent of internal damage of the graphite nodules corresponds to the state of the crack tip plastic zone when it intersects or encompasses the nodules. In specimens tested at 720 or 800 °C, nodules have suffered a significant degree of decarburization as shown in Figure 2.23b. At these temperatures, nodules have a porous appearance due to the depletion of carbon.

Examination of the longitudinal cross-sections shows that the fatigue region tends to be fairly flat and transgranular in the specimens tested at the lower strain ranges. Optical microscope images are shown in Figure 2.25a to Figure 2.25f for the same specimens examined in the preceding discussion. Extensive intergranular damage is seen at 400 °C, where the embrittlement mechanism is active. The significant presence of magnesium on the fracture surface, combined with the presence of intergranular fracture throughout the cross-section at this temperature, suggests that the embrittlement which was discussed in Section 2.3.3.1 also contributed to the fatigue failure at 400 °C. *Yanagisawa et al.* (1980) and *Wu et al.* (2013) similarly found that specimens tested in low cycle fatigue at 400 °C failed due to a high degree of intergranular damage which was also attributed to the embrittlement phenomenon.

Intergranular fracture is also present in the longitudinal cross-section of a specimen tested at 800 °C, where the high temperature mechanisms of creep and oxidation are very active at the grain boundaries. As seen in Figure 2.25f, some oxide has penetrated

the specimen surface and fracture surface along grain boundaries which would have weakened their resistance to fracture. However, extensive intergranular damage is also present in the bulk of the material which is due to creep damage, rather than oxidation.

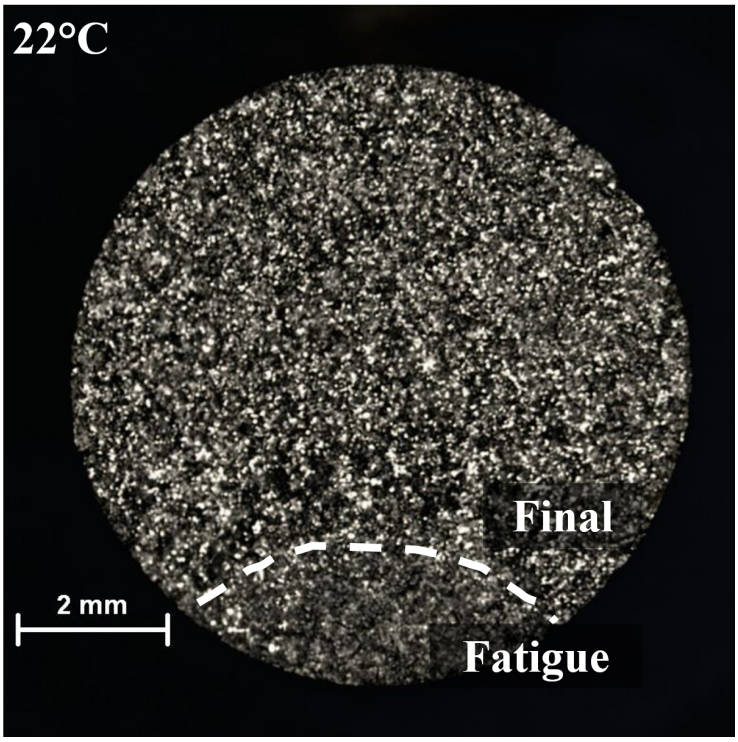

(a)

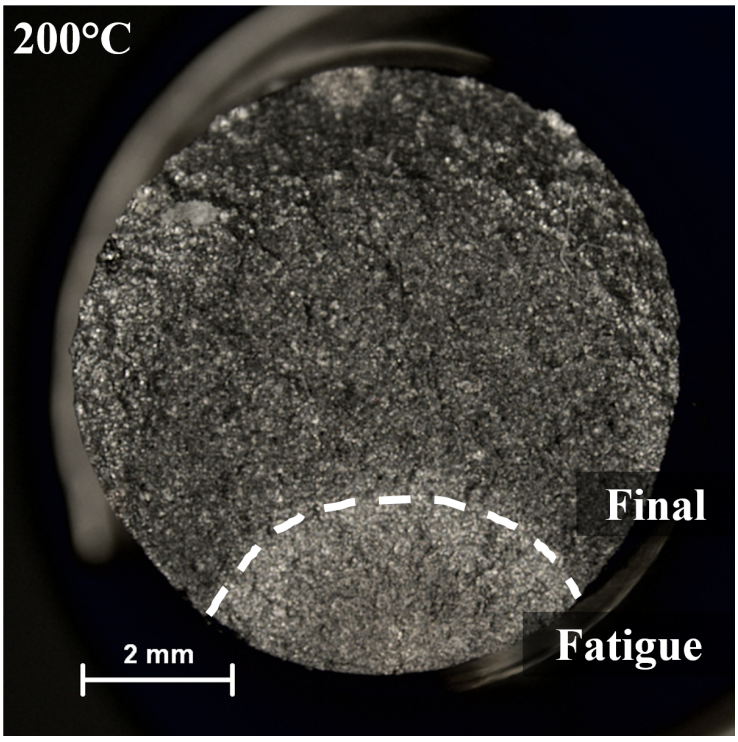

(b)

Figure 2.18: Optical microscope images of the fracture surfaces obtained from LCF tests at a low strain range at (a) room temperature and (b) 200 °C. Continued on next page, (c) 400 °C, (d) 600 °C, (e) 720 °C and (f) 800 °C.

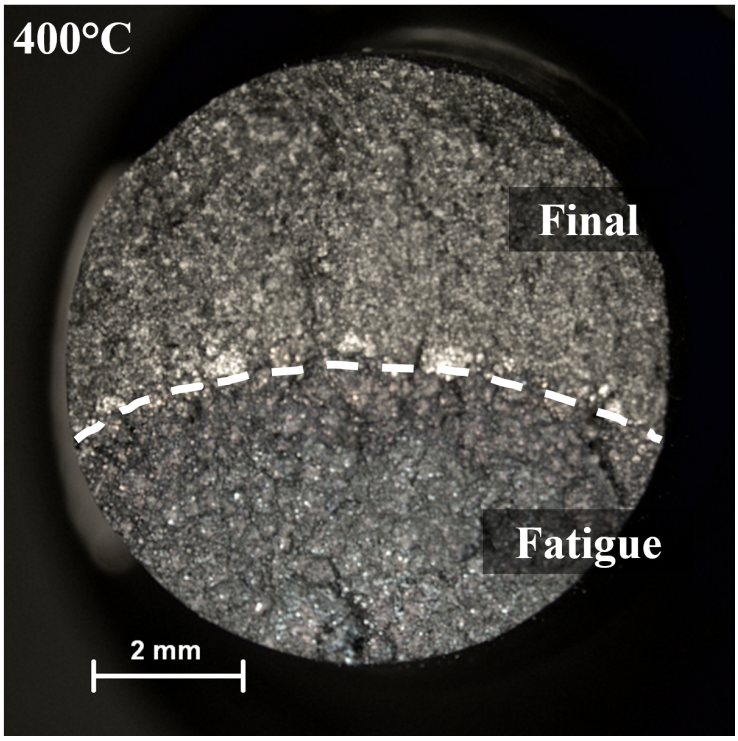

(c)

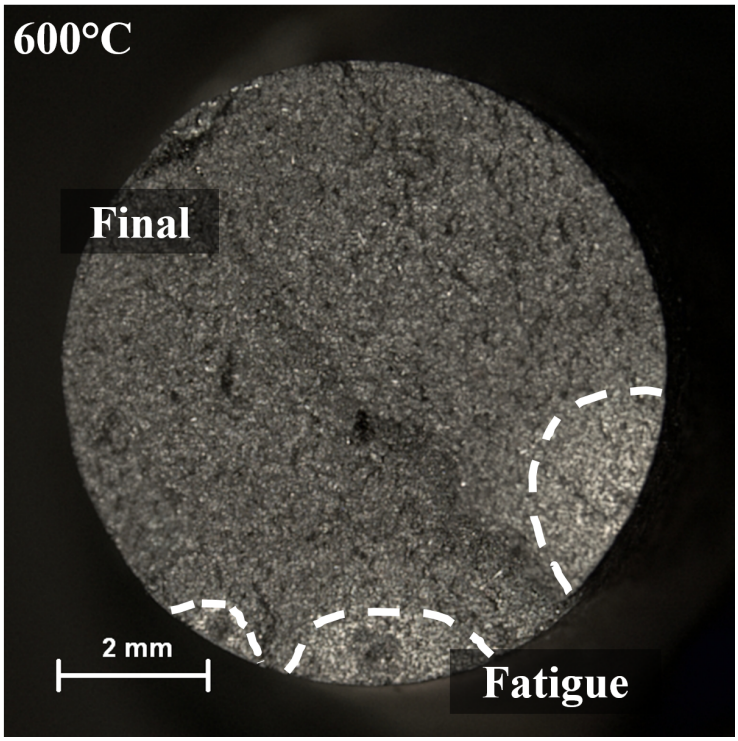

(d)

Figure 2.18: Continued from previous page.

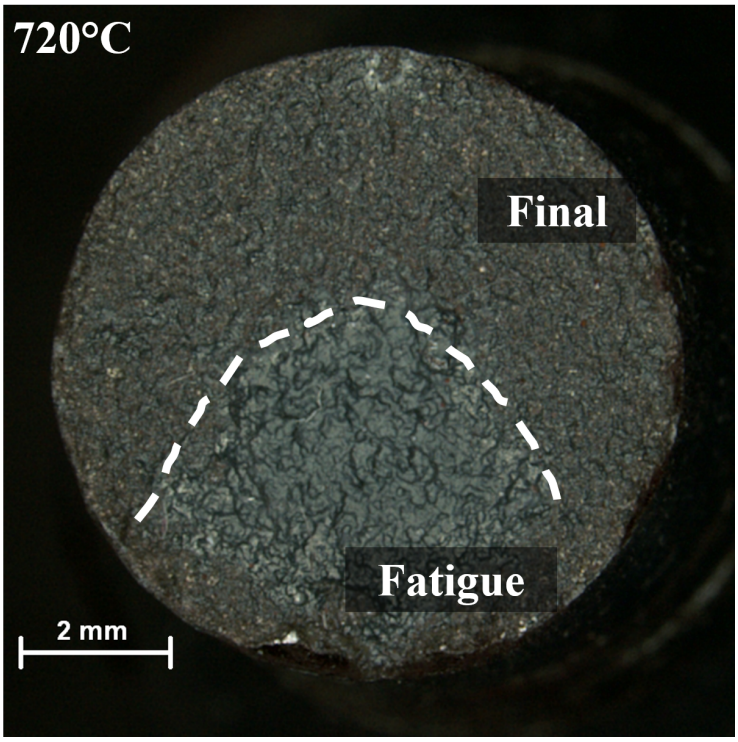

(e)

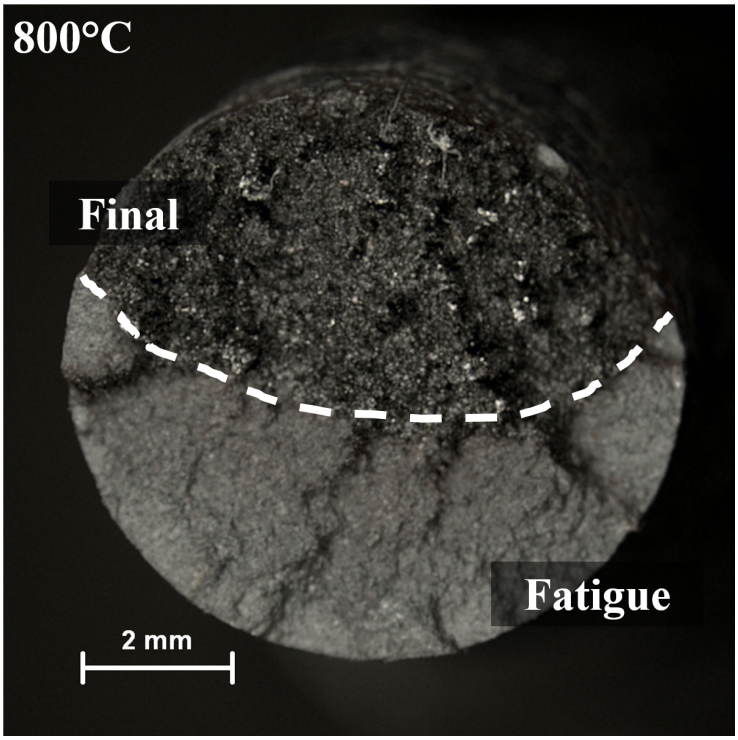

(f)

Figure 2.18: Continued from previous page.

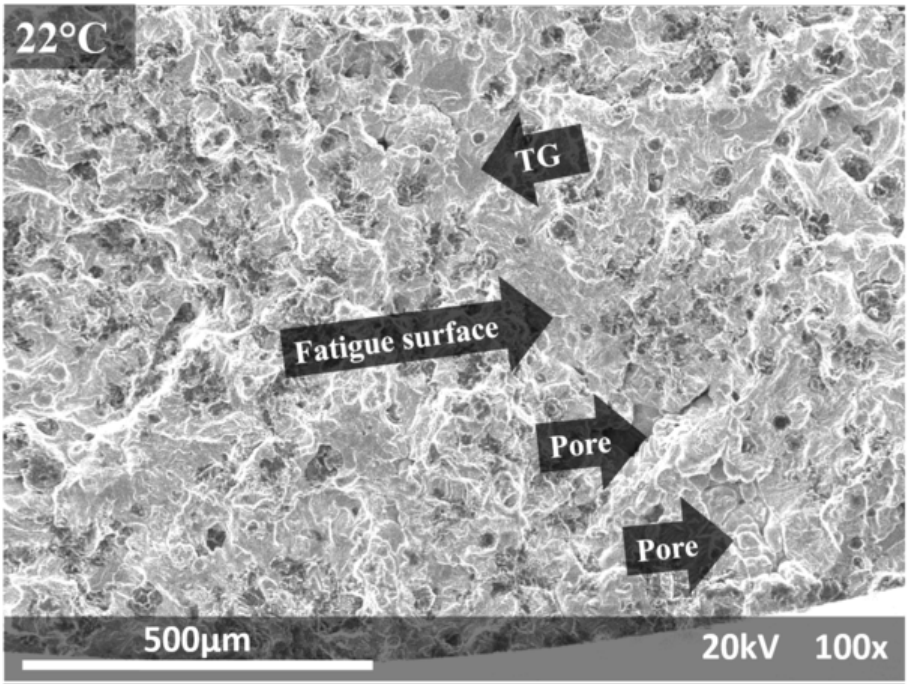

(a)

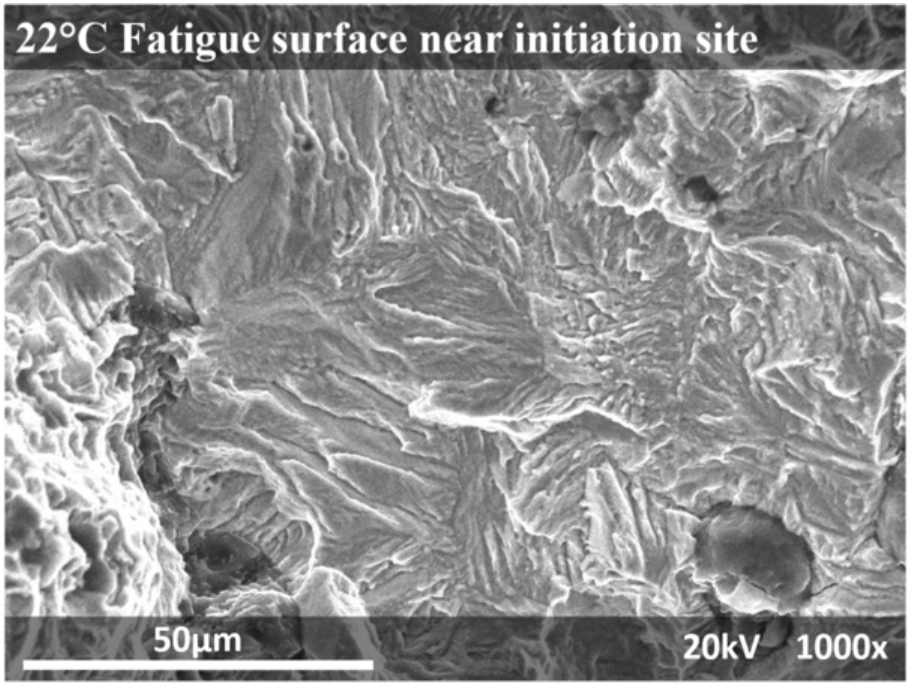

(b)

Figure 2.19: SEM images of (a) the crack initiation site in a specimen tested under LCF at 22 °C for a low strain range and (b) fatigue surface near site of crack initiation.

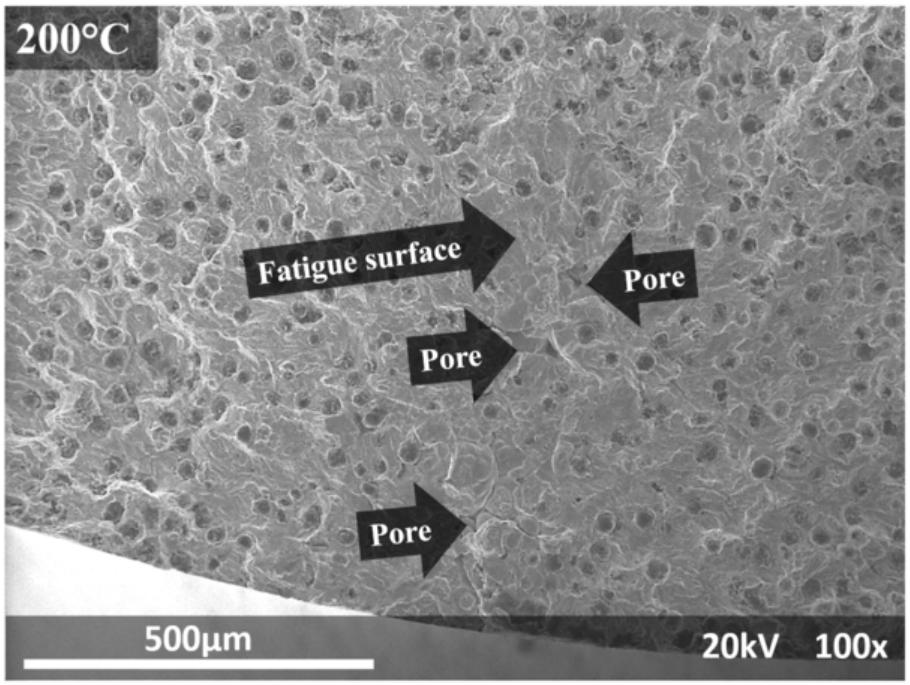

(a)

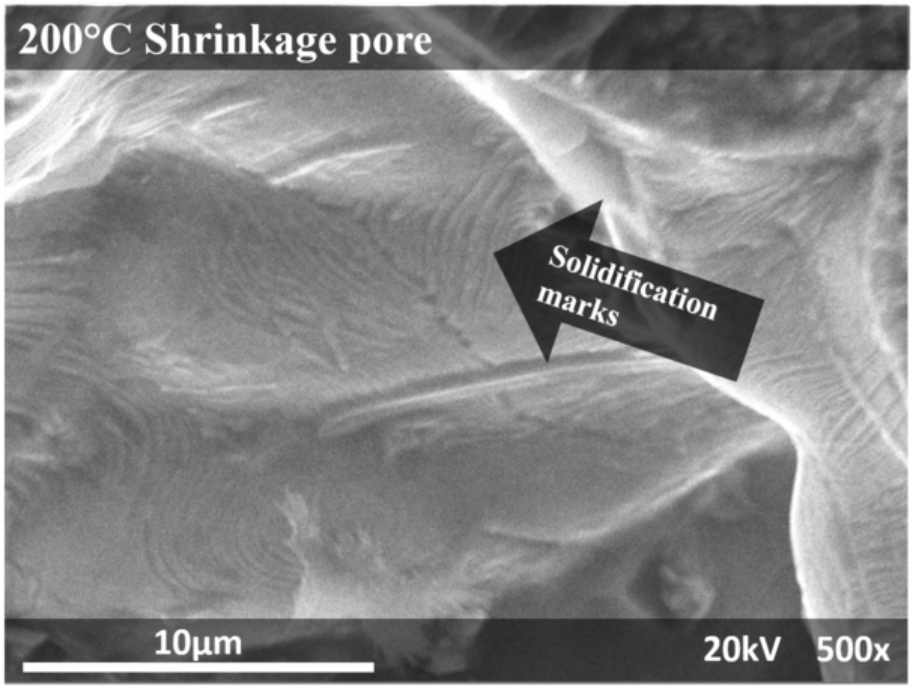

(b)

Figure 2.20: SEM images of (a) the crack initiation site of a specimen tested under LCF at 200 °C for a low strain range and (b) shrinkage pore at site of crack initiation. Continued on next page, SEM image of (c) fatigue fracture near initiation site.

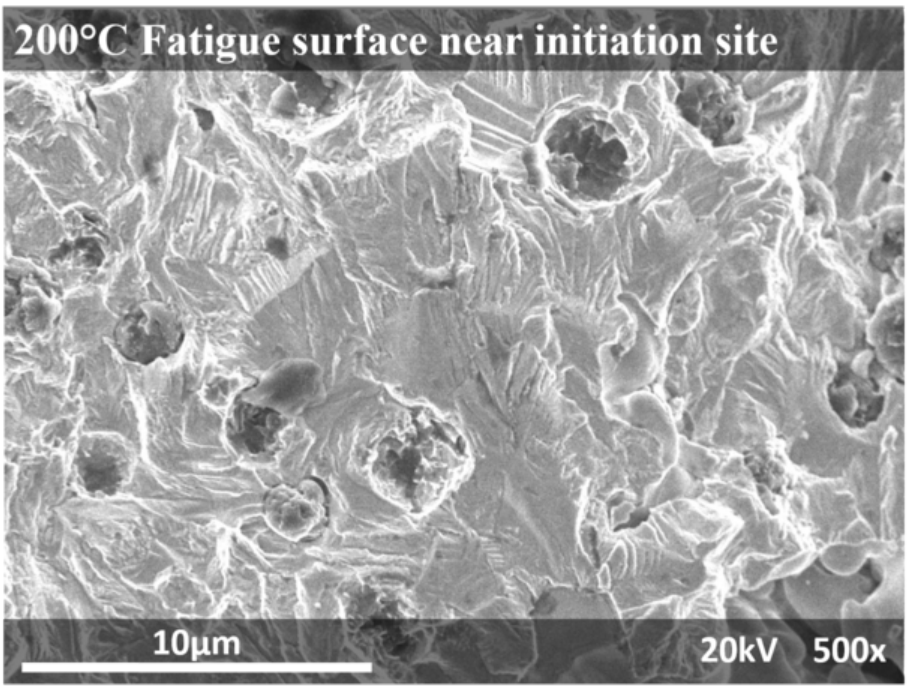

(c)

Figure 2.20: Continued from previous page.

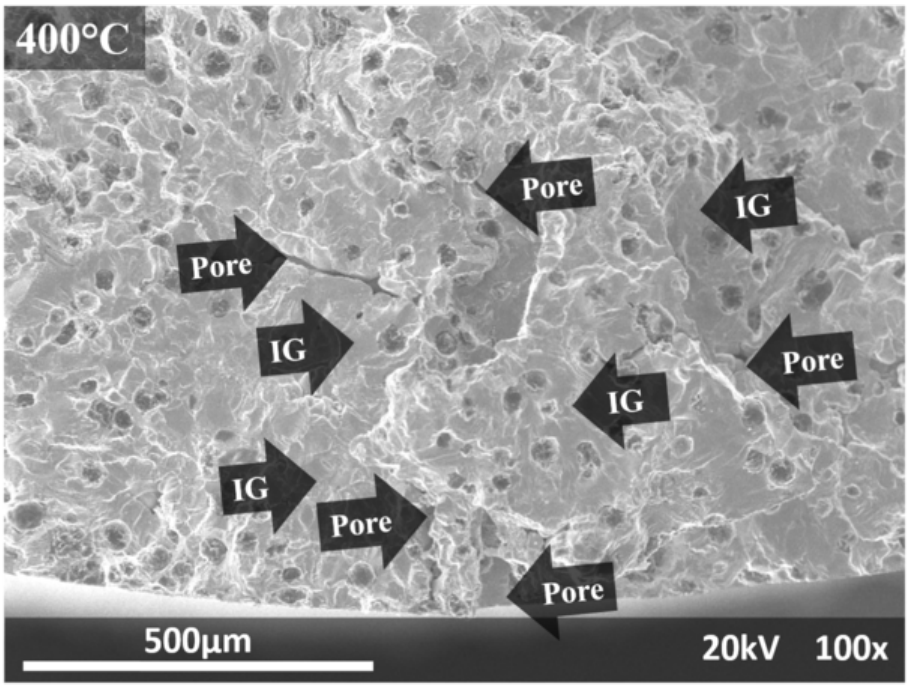

(a)

(b)

Figure 2.21: SEM images of (a) the site of crack initiation of a specimen tested under LCF at 400 °C for a low strain range and (b) shrinkage pore at site of crack initiation. Continued on next page, SEM image of (c) brittle intergranular fracture near initiation site.

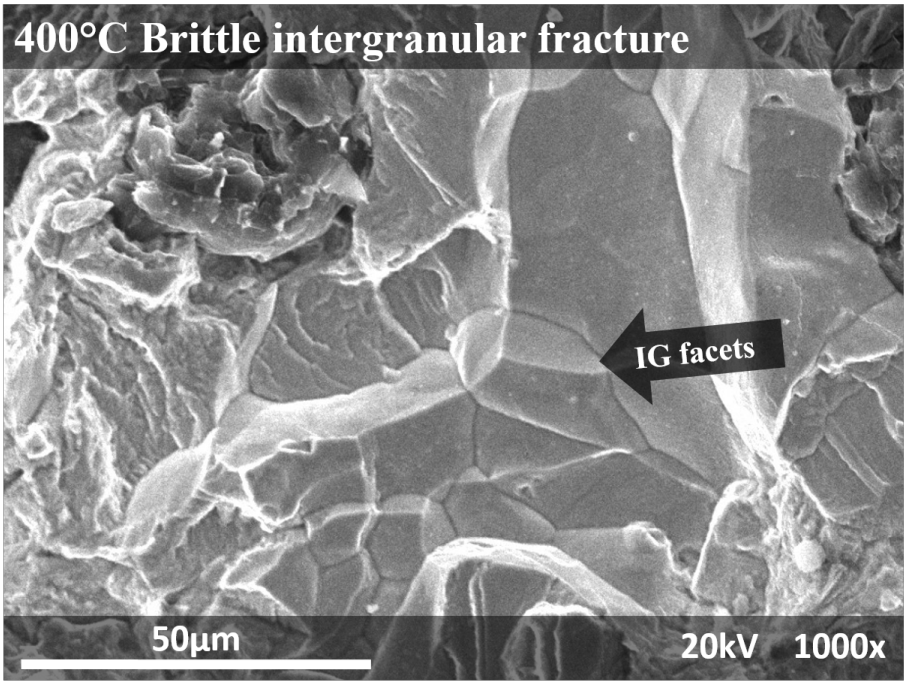

(c)

Figure 2.21: Continued from previous page.

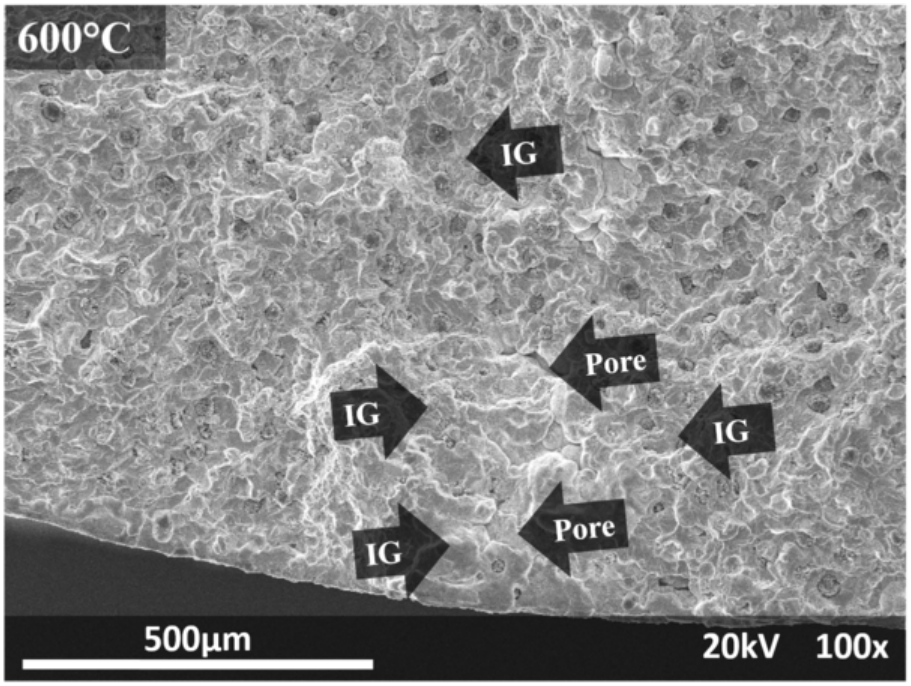

Figure 2.22: SEM images of a crack initiation site of a specimen tested under LCF at 600 °C for a low strain range.

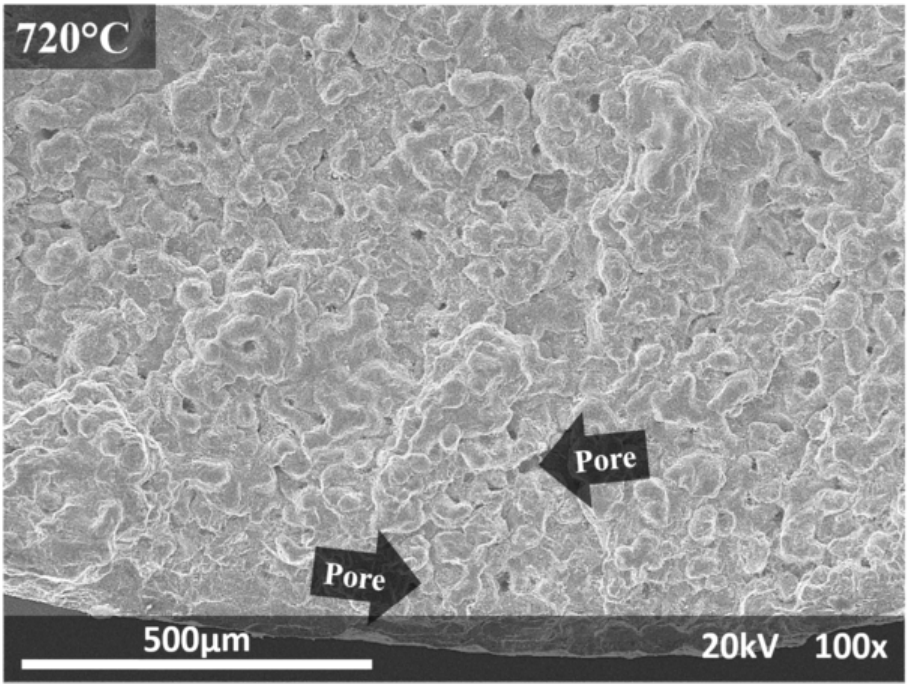

(a)

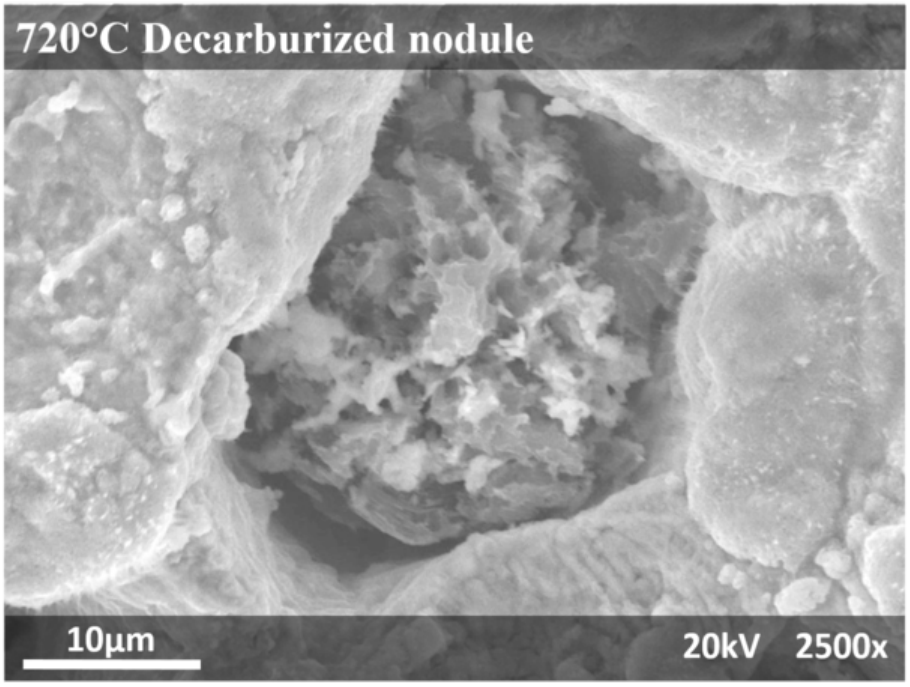

(b)

Figure 2.23: SEM images of (a) a crack initiation site of a specimen tested under LCF at 720 °C for a low strain range and (b) a decarburized graphite nodule.

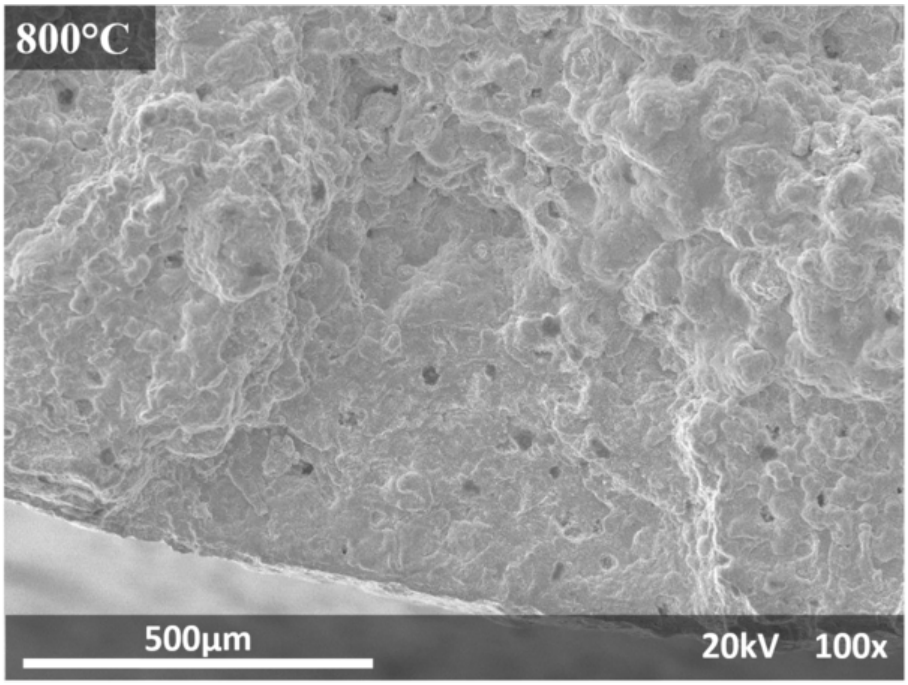

Figure 2.24: SEM images of a crack initiation site of a specimen tested under LCF at 800 °C for a low strain range.

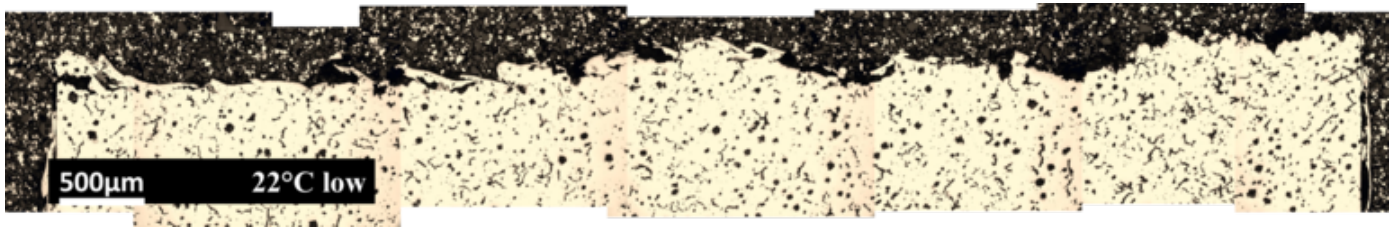

(a)

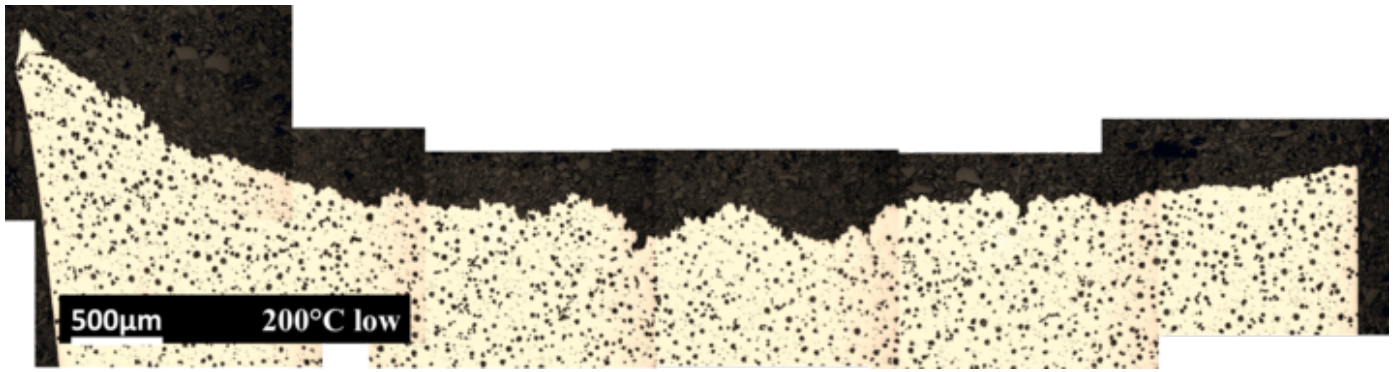

(b)

Figure 2.25: Optical micrographs of longitudinal cross-sections through the fracture surface in specimens tested at a low strain range under low cycle fatigue at (a) room temperature and (b) 200 °C. Continued on next page, (c) 400 °C, (d) 600 °C, (e) 720 °C and (f) 800 °C.

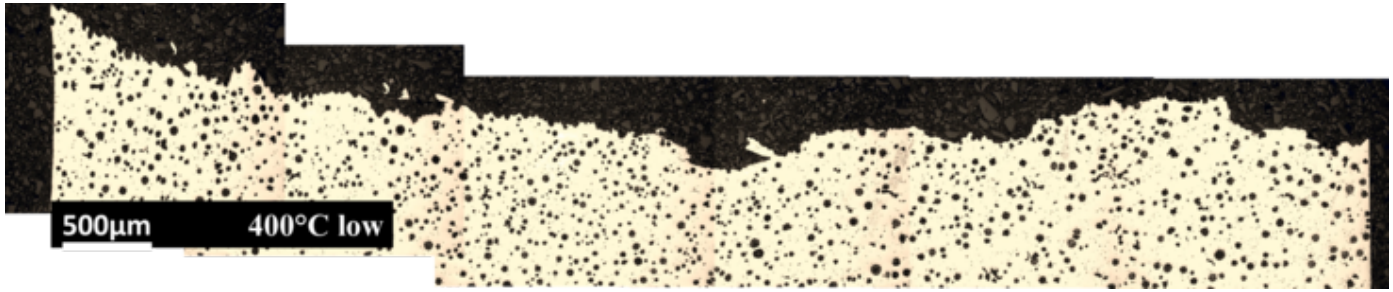

(c)

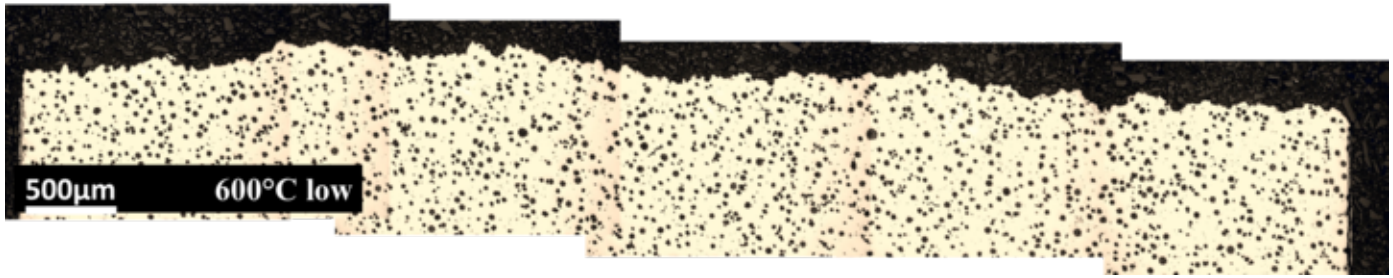

(d)

Figure 2.25: Continued from previous page.

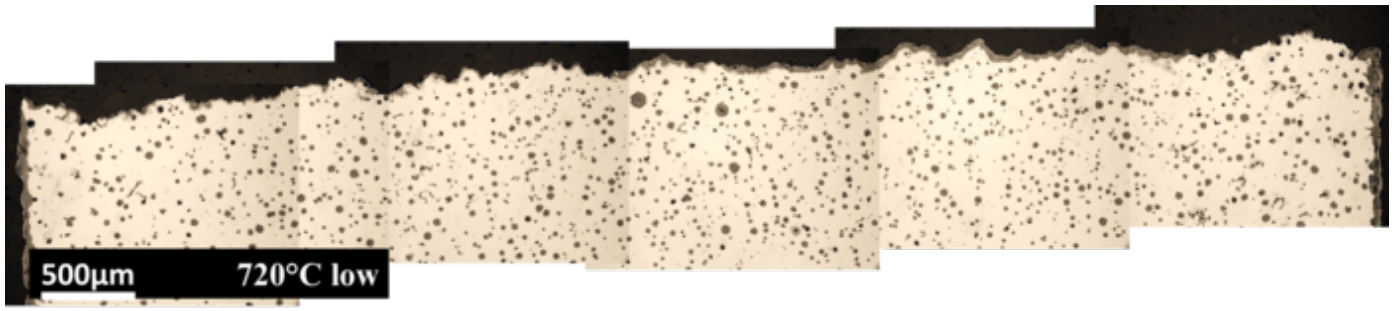

(e)

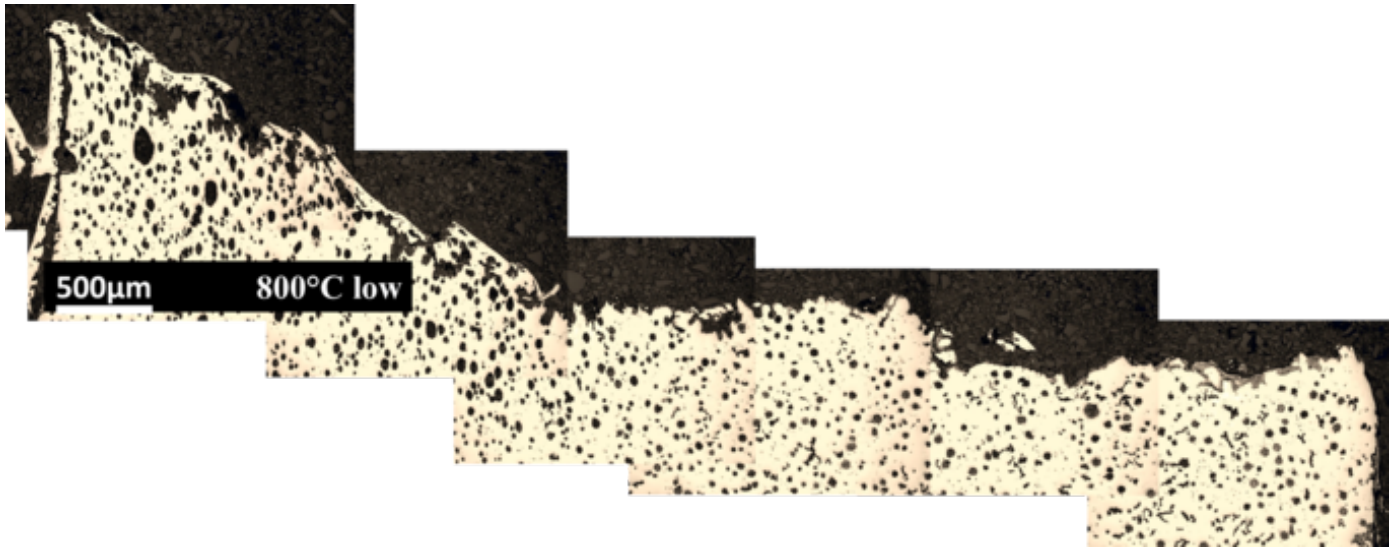

(f)

Figure 2.25: Continued from previous page.

When the strain range is increased, the fracture surfaces have a drastically different appearance than those created at low strain ranges. Rather than featuring a clear region of fatigue crack growth, the fracture surfaces at high strain ranges tend to be uniform in appearance, with no clear crack initiation site(s). Figure 2.26 shows the fracture surfaces from specimens tested under isothermal fatigue from room temperature up to 800 °C. The surfaces are generally reflective due to the extensive presence of cleavage facets on the surface.

At room temperature and 200 °C, fracture occurs in a predominantly transgranular manner, as shown in Figure 2.27a and Figure 2.28a. The majority of nodules at the fracture surface have suffered extensive damage through the nucleus of the nodule, as illustrated in Figure 2.27b. Near some of the nodules, the fracture surface has a similar appearance to that observed in Figure 2.19b for the fatigue surface near the site of crack initiation. However, the remainder of the fracture surface has the appearance of brittle transgranular cleavage, which is shown in Figure 2.27c. Based on these observations, it is proposed that the fatigue crack at high strain ranges initiates due to damage in the graphite nodules fairly uniformly through the cross-section.

At 400 °C, intergranular fracture is predominant, as shown in Figure 2.29a. Intergranular facets, shown in Figure 2.29b, are readily observed on the fracture surface. Chemical analysis conducted via EDS showed a significant presence of magnesium on the fracture surface. These observations suggest that 400 °C embrittlement contributed to the fatigue failure at high strain ranges at 400 °C, as well as the low strain ranges, as previously discovered. Numerous shrinkage pores, shown in Figure 2.29c are present on the surface. Interestingly, ductile transgranular fracture is also present throughout the fracture surface, as confirmed by the presence of dimples shown in Figure 2.29d. Small regions of intergranular fracture are dispersed over the entire fracture surface which are surrounded by ductile transgranular fracture. This indicates that many small fatigue cracks initiated throughout the cross-section, and the

remaining material ligaments suffered ductile final failure.

At 600 °C and higher, the fracture surfaces have the appearance of mixed transgranular and intergranular fracture, as shown in Figure 2.30, Figure 2.31 and Figure 2.32, respectively. A thin oxide is present which partially obscures the features of the fracture surfaces. However, at these temperatures, decarburization of the nodules occurs throughout the fracture surface.

Longitudinal cross-sections at the fracture surface are shown for specimens tested at high strain ranges from room temperature up to 800 °C in Figure 2.33a to Figure 2.33f. Intergranular fracture is prevalent at 400 °C, where the embrittlement is active, and also at 800 °C, where creep and oxidation can contribute damage to the grain boundaries. By comparing the topography of the fracture surface between specimens tested at the low and high strain ranges within a temperature, it is clear that the low strain range creates a fairly flat, transgranular region of fatigue crack growth that becomes increasingly intergranular as the crack propagates. At the high strain range, however, intergranular fracture is important to crack nucleation and propagation.